

Reconciling Surface Deflections From Simulations of Global Mantle Convection

Conor P. B. O’Malley^{1,2}, Gareth G. Roberts¹, James Panton³, Fred D. Richards¹, J. Huw Davies³, Victoria M. Fernandes^{1,4}, Sia Ghelichkhan⁵

¹Department of Earth Science & Engineering, Imperial College London, London SW7 2BP, UK

²now at Cathie Group, 2-4 Hanover Square, Newcastle upon Tyne, NE1 3NP, UK

³School of Earth & Environmental Sciences, University of Cardiff, Park Place, Cardiff CF10 3AT, UK

⁴now at Section 4.6 Geomorphology, GFZ Potsdam, Telegrafenberg, 14473 Potsdam, Germany

⁵Research School of Earth Sciences, Australian National University, 142 Mills Road, Acton, ACT 0200,

Australia

Key Points:

- Numeric and analytic predictions of surface deflections from mantle convection simulations are compared.
- Impact of gravitation, excising shallow structure, boundary conditions, and different viscosity and density distributions are quantified.
- Calculated effective contributions to surface deflection emphasize dominance of upper mantle structure.

Corresponding author: Conor O’Malley; Gareth Roberts, c.omalley1@msn.com;
gareth.roberts@imperial.ac.uk

Abstract

The modern state of the mantle and its evolution on geological timescales is of widespread importance for the Earth sciences. For instance, it is generally agreed that mantle flow is manifest in topographic and drainage network evolution, glacio-eustasy and in the distribution of sediments. There now exists a variety of theoretical approaches to predict histories of mantle convection and its impact on surface deflections. A general goal is to make use of observed deflections to identify Earth-like simulations and constrain the history of mantle convection. Several important insights into the role of radial and non-radial viscosity variations, gravitation, and the importance of shallow structure already exist. Here we seek to bring those insights into a single framework to elucidate the relative importance of popular modelling choices on predicted instantaneous vertical surface deflections. We start by comparing results from numeric and analytic approaches to solving the equations of motion that are ostensibly parameterised to be as-similar-as-possible. Resultant deflections can vary by $\sim 10\%$, increasing to $\sim 25\%$ when viscosity is temperature-dependent. Including self-gravitation and gravitational potential of the deflected surface are relatively small sources of discrepancy. However, spherical harmonic correlations between model predictions decrease dramatically with the excision of shallow structure to increasing depths, and when radial viscosity structure is modified. The results emphasise sensitivity of instantaneous surface deflections to density and viscosity anomalies in the upper mantle. They reinforce the view that a detailed understanding of lithospheric structure is crucial for relating mantle convective history to observations of vertical motions at Earth's surface.

Plain Language Summary

Flow of rock within Earth's interior plays a crucial role in evolving the planet. It moves heat and chemicals from deep depths to the surface, for instance. It also moves the lithosphere—the Earth's outer rocky shell—which in turn impacts processes including mountain building, sea-level change, formation of volcanoes, river network evolution, and natural resource distribution. Consequently, we wish to understand the present state, and history, of flowing rock within Earth's interior. Observations exist to address this problem, and mathematics and computing tools can also be used to predict histories of flow and their impact on Earth's surface. We explore how assumptions incorporated into such numeric models can affect calculations of the vertical deflection of Earth's surface. Predictions from different models are compared, with a view to identifying crucial modelling components. Surface sensitivity to deep flow is assessed, demonstrating how surface observations can enlighten flow histories.

1 Introduction

Mantle convection plays a crucial role in Earth's evolution (e.g., Hager & Clayton, 1989; Parsons & Daly, 1983; Pekeris, 1935). It is well understood, for instance, that flow in the mantle is fundamental in the transfer of heat and chemicals from the deep Earth to the surface, in driving horizontal and vertical lithospheric motions (thus tectonic processes), and in magnetism via interactions with the core (e.g., Biggin et al., 2012; Davies et al., 2023; Foley & Fischer, 2017; Hoggard et al., 2016; Holdt et al., 2022; Pekeris, 1935). In turn, many processes operating at or close to Earth's surface are impacted, including glacio-eustasy, magmatism, climate, sediment routing, natural resource distribution, drainage network evolution, and development of biodiversity (e.g., Bahadori et al., 2022; Ball et al., 2021; Braun, 2010; Chang & Liu, 2021; Hazzard et al., 2022; O'Malley et al., 2021; Salles et al., 2017; Stanley et al., 2021). Clearly, understanding the physical and chemical evolution of the mantle has broad implications. An important goal is to determine contributions to surface processes from the modern mantle and its history during, say, the last 100 million years.

68 Residual oceanic age-depth measurements, potential field data, seismic tomographic
 69 models and melting histories of young mafic rocks are providing increasingly coherent
 70 observational insights into the modern and recent state of the mantle (e.g., Ball et al.,
 71 2022; Davies et al., 2023; Fichtner et al., 2009, 2013; Fichtner & Villaseñor, 2015; French
 72 & Romanowicz, 2015; Hoggard et al., 2016; Holdt et al., 2022; Kaula, 1963; Lekić & Fischer,
 73 2014; Priestley & McKenzie, 2013; F. D. Richards et al., 2021). Stratigraphic and
 74 geomorphic observations as well as magmatic histories provide clues about the history
 75 of mantle convection on geologic timescales (e.g., Al-Hajri et al., 2009; Czarnota et al.,
 76 2013; Flament et al., 2015; Fernandes et al., 2019; Fernandes & Roberts, 2021; Galloway
 77 et al., 2011; Gunnell & Burke, 2008; Gurnis et al., 2000; Hoggard et al., 2021; Lambeck
 78 et al., 1998; Morris et al., 2020; O’Malley et al., 2021; Stanley et al., 2021). Despite these
 79 advances, observations providing information about the history of mantle convection are
 80 sparse in places, especially within continental interiors and back in time (see e.g., Hog-
 81 gard et al., 2021). Moreover, disentangling contributions from crustal, lithospheric and
 82 sub-lithospheric processes to surface deflections remains challenging and controversial
 83 (see e.g. Hoggard et al., 2021; Wang et al., 2022).

84 Theoretical approaches that retrodict histories of mantle convection can, in prin-
 85 ciple, be used to fill in spatio-temporal gaps in the observational record and disentan-
 86 gle contributions to surface observables from different geologic processes (e.g., Baumgard-
 87 ner, 1985; Bunge & Baumgardner, 1995; Davies et al., 2013; Flament et al., 2015; Ghe-
 88 lichkhan et al., 2021; Hager et al., 1985; Moucha & Forte, 2011; Steinberger & Antret-
 89 ter, 2006). Increasingly realistic geodynamic simulations incorporating, for instance, plate
 90 motions, gravitation and deflection of gravitational potential fields, complex rheologies,
 91 viscosity laws that can include temperature, pressure, composition, grain size and strain
 92 rate dependence, and assimilation of seismic tomographic information into flow solutions,
 93 result in a diverse array of retrodicted flow histories. Mineralogical phase changes, com-
 94 pressibility, different surface and core-mantle boundary slip conditions (e.g., no-slip, free-
 95 slip), chemical and thermal buoyancy, and plate motion constraints on mantle structure
 96 can also generate diverse predictions of mantle convection and resultant surface deflec-
 97 tions (e.g., Baumgardner, 1985; Bunge et al., 2002, 2003; Corrieu et al., 1995; Crameri
 98 et al., 2012; Dannberg et al., 2017; “Topographic asymmetry of the South Atlantic from
 99 global models of mantle flow and lithospheric stretching”, 2014; Forte, 2007; Ghosh &
 100 Holt, 2012; Glišović & Forte, 2016; Hager & Clayton, 1989; Heister et al., 2017; Liu &
 101 Gurnis, 2008; Panasyuk et al., 1996; Ribe, 2007; Ricard, 2007; Tackley et al., 1993; Zhong
 102 et al., 2008; Zhou et al., 2018). Aside from the fundamental choice of governing equa-
 103 tions and parameterizations underpinning simulations, mathematical and computational
 104 approaches to solve the equations of motion generate different predictions of surface de-
 105 flections. These approaches sit within two broad families: numeric simulations (e.g., AS-
 106 PECT, CitcomS, TERRA; Bangerth et al., 2023; Baumgardner, 1985; Zhong et al., 2000),
 107 and propagator-matrix-based, quasi-analytic techniques, that can be solved in two or three
 108 dimensions, and importantly for our purposes, spherically and spectrally (e.g., Colli et
 109 al., 2016; Hager & O’Connell, 1979; Parsons & Daly, 1983).

110 A challenge then is to establish whether observed surface deflections can be used
 111 to discriminate between theoretical predictions of mantle convection, and, in turn, iden-
 112 tify models that generate realistic and testable retrodictions. In this study we are prin-
 113 cipally concerned with establishing similarities and sensitivities of predicted instanta-
 114 neous vertical surface deflections. We focus on vertical motions for two reasons. First,
 115 inventories of measurements of uplift and subsidence—on timescales of mantle convection—
 116 now exist for most continents and could be compared to predictions from global simu-
 117 lations in future work (e.g. Fernandes & Roberts, 2021, and references therein). Secondly,
 118 many geodynamic simulations incorporate horizontal motions of the lithosphere, which
 119 limits their use as a comparator.

From an observational perspective, it would be useful to establish rules-of-thumb that quantify sensitivity of surface deflections to choices made when predicting them. Many such rules are already well known from analytic and numeric solutions of the equations of motion (e.g., Colli et al., 2016; Hager & O'Connell, 1979; Holdt et al., 2022; Lees et al., 2020; Parsons & Daly, 1983). For instance, a suite of benchmark studies exist that compare predictions from numeric mantle convection simulations with analytic solutions (see e.g., Bauer et al., 2019; Kramer et al., 2021; Zhong et al., 2008, and references therein). Those papers tend to focus on establishing the fidelity of numeric models. In contrast, our goals are to, first, understand how calculated deflections are impacted by the choice of methodology used to solve the equations of motion and, secondly, to establish sensitivities to popular assumptions incorporated into simulations. We want to know the extent to which an improved fit between predictions and observations reflects a more Earth-like density and viscosity structure versus modelling choices. Our thesis is that performing all tests in a self-consistent framework, as we do in this study, provides a straightforward way to collate insights into the sensitivities of predicted surface deflections and to simplify the comparison of predictions from different suites of models.

1.1 Our Approach and Paper Structure

We start by exploring the consequences of solving the equations of motion numerically, using the TERRA software, and analytically, using Ghelichkhan et al. (2021)'s propagator matrix algorithms (see Figure 1 & Supporting Information). We make use of the flexibility of numeric approaches by incorporating a variety of assumptions and parameterizations that are not amenable to analytic attack (e.g., temperature-dependent viscosity). All numeric simulations presented in this paper were driven by the plate motion history of Merdith et al. (2021, see Figures 1g–h and S1). The models have a resolution of 60 km at their surface (see Supporting Information for details of model setup and execution). We note that they do not directly assimilate information about the mantle from tomographic models. Ensuring that numeric simulations are accurate and stable means that computational burden is often considerable and hence systematic exploration of parameter space remains challenging. In contrast, analytic approaches can yield calculated surface deflections that are (mathematically) accurate, whilst including features such as radial gravitation, with much less computational cost. Consequently, we make use of propagator matrix techniques to explore parameter space, examine benchmarks, and reproduce results. We establish the sensitivity of solutions to different parameterizations and approaches to solving the equations of motion.

There are at least two important considerations when solving the equations of motion analytically. First, solutions are only known to exist in the spherical harmonic domain for fluid bodies with radial viscosity (i.e., no lateral variability in viscosity). Second, generating solutions in the spherical harmonic domain places practical limits on spatial resolution of solutions. Consider that the number of spherical harmonic coefficients per degree = $2l+1$, where l is degree, so for a given maximum degree L , there are $(L+1)^2$ coefficients in total. For instance, when $L = 50$ there are 2,601 coefficients for each model. Consider also that spatial resolution increases approximately with the reciprocal of l (see Section 2.2). Incorporating full resolution output from the numeric models (60 km at the surface) would require $L \approx 880$, with 776,161 coefficients, which is computationally cumbersome. Furthermore, observational constraints on mantle-related surface deflection are unlikely to be finer than the flexural wavelength of the overlying lithosphere, $l \approx 50$ (e.g., Holdt et al., 2022). With these limitations in mind, we compared surface deflections predicted using different approaches at the same resolution up to $l = 50$ (see Supporting Information and Section 2.3).

Most of the tests in this paper compare surface deflections calculated using the entirety of the model domains (i.e., from CMB to the surface). This approach simplifies like-for-like comparisons of model predictions and comparisons to increasingly complex

scenarios. However, amplitudes of calculated deflections will of course not reflect estimated amplitudes of dynamic topography. This approach purposefully avoids isolating passive or plate-driven surface deflections and sub-plate support from numeric simulations or analytic solutions. Since the central focus of this work is merely on quantifying contrasts that arise from choices made when simulating mantle convection, we wish to avoid incorporating additional modifications where possible. In subsequent tests we examine the consequences of simply removing shallow structure, a widely used approach for estimating dynamic support from simulations (see e.g., Flament et al., 2013; Flament, 2018; Wang et al., 2022).

With this framework in place we generate, compare and contrast predicted surface deflections. The first suite of tests are purposefully simple, e.g., incompressible, constant gravitational acceleration (no self-gravitation or radial variation in gravitation) and have radial viscosity independent of temperature. Results are compared to estimates of sub-plate support from oceanic age-depth residuals with a view to quantifying corrections necessary to convert predicted instantaneous surface deflections into estimates of sub-plate support. We then systematically examine the impact of incorporating radial variations in gravitational acceleration, contribution to flow from deflection of the gravitational potential field, removal of shallow density structure, choice of surface and CMB slip conditions, inclusion of temperature-dependent viscosity, and amplification or reduction of viscosity and density anomalies in the upper and lower mantle (Section 4; Tables 1–2). A closed-loop modelling strategy is explored in which predicted surface deflections from these relatively complex models are compared to results from simpler reference models. Finally, a methodology for assessing effective contributions to surface topography from mantle anomalies is presented.

2 Numeric and Analytic Calculations of Surface Deflection

The Supporting Information document summarises the formulations of Stokes' equations that are solved, model parameter values used and the numeric approach to calculating mantle convection using the TERRA finite-element software. Here, we move straight to explaining how those simulations are used to calculate radial stresses, σ_{rr} , thence vertical deflections, h , at Earth's surface (Figure 1). A methodology for representing model predictions in the spherical harmonic domain is then described. We then examine analytic solutions obtained using propagator matrix techniques.

2.1 Deflections calculated using radial stresses from numeric simulation

Following Parsons and Daly (1983), surface deformation is estimated from numeric simulations of mantle convection by making use of the requirement that normal stress is continuous across the upper boundary of the solid Earth (see also McKenzie, 1977; Ricard, 2015). In other words, radial stresses generated by the solid Earth are required to be balanced by stresses generated by the overlying (oceanic or atmospheric) fluid. There are three contributions to normal stress at this boundary from the mantle: hydrostatic stress that would exist even in the absence of convection, dynamic stress arising from convection, and viscous stress which opposes fluid motion (see Equations 2–6 in Supporting Information). To satisfy the continuity condition, these stresses must be balanced by those generated by the water (or air) column atop this boundary. If the pressure from the overlying column is hydrostatic, the resultant condition is

$$\rho_w g_s h = \rho_m g_s h + \sigma_{rr}, \quad (1)$$

where σ_{rr} incorporates deviatoric viscous stresses generated by mantle convection and dynamic pressure ($\sigma_{rr} = \tau_{rr} - p$), obtained by solving Equation 2 in Supporting Information. In practice, since values for this term are obtained by subtracting radial litho-

static stress from the total stress, values of σ_{rr} integrate to zero globally. g_s is gravitational acceleration at Earth's surface, ρ_m is the mean density for the surficial layer, and ρ_w is the density of the overlying fluid (see Table S1). Note that we do not impose additional oceanic plate cooling, e.g., due to hydrothermal circulation at ridges. Cooling and subsequent subsidence, as well as passive return flow at ridges, arise naturally from solution of the governing equations laid out in Section 2 of Supporting Information.

Surface deflection arising in response to predicted convective flow, h , is approximated by rearranging Equation 1,

$$h \approx -\frac{\sigma_{rr}}{(\rho_m - \rho_w)g_s}. \quad (2)$$

Deflections are estimated from radial stresses at times of interest (e.g., the present-day) by re-running one time-step of the TERRA model. During that time-step, a free-slip boundary condition, for which analytic approximations for surface deflection exist, is imposed instead of the plate-slip condition prescribed during the main model run routine (see Section 2.3; Ricard, 2015). The numeric models themselves apply a quasi-rigid condition at the surface, whereby flow is driven by estimates of real plate velocities (from Merdith et al., 2021), and so the surface layers behave as a series of rigid, laterally mobile plates rather than a single rigid shell. We assess the accuracy of modifying boundary conditions in this way by converting calculated deflections into the spherical harmonic domain and comparing them to predictions generated using the analytic propagator matrix approach. The consistent boundary flux (CBF) method provides an alternative means to accurately calculate normal stresses (Zhong et al., 1993). Previous benchmarking with TERRA has shown mean errors of a few percent or less for surface deflection predictions at low harmonic degrees, $l \leq 16$ (Davies et al., 2013).

2.2 Surface Deflections Calculated in the Spherical Harmonic Domain

Transforming stress, or surface deflections, calculated using numeric approaches into the frequency domain provides straightforward means of comparing results to analytic solutions and of quantifying spectral power, i.e., the magnitude of contribution to the total signal from different wavelengths. Since the models that we investigate are global in scope, we do so using spherical harmonics. The methodology for calculating spherical harmonics and the definition of power adopted in this study are included as Supporting Information. Figure 2 shows an example of surface stresses calculated using the TERRA code, their spherical harmonic representation, calculated surface deflections in the spherical harmonic domain, and associated statistics and power spectra.

Using the total power per degree convention, Hoggard et al. (2016) derived a rule-of-thumb for estimating the power spectrum of dynamic topography (see their Supporting Information), P_l^{DT} , using Kaula (1963)'s approximation for the long-wavelength gravity field of Earth as a function of l :

$$P_l^{DT} \approx \left(\frac{GM}{ZR^2} \right)^2 \left(\frac{2}{l} - \frac{3}{l^2} + \frac{1}{l^4} \right), \quad (3)$$

where G is the gravitational constant, $M = 5.97 \times 10^{24}$ kg is the mass of the Earth, $R \approx 6370$ km is Earth's radius. The value of low-degree admittance, Z , between gravity and topography varies as a function of viscosity, as well as the depth and wavelength of internal density anomalies (Colli et al., 2016). Hoggard et al. (2016) found that assuming an average value of $Z = 12$ mGal km⁻¹ provides a reasonable approximation of observed residual topographic trends, thus we make use of that value in the remainder of the paper. Finally, it is useful to note that Jeans (1923) related spherical harmonic degree to wavelength λ , which at Earth's surface can be approximated via $\lambda \approx 2\pi R / \sqrt{l(l+1)}$.

263 **2.3 Surface Deflections Calculated Analytically**

264 The second methodology used to calculate surface deflection in response to man-
 265 tle convection is the analytic propagator matrix technique (e.g., Craig & McKenzie, 1987;
 266 Gantmacher, 1959; Ghelichkhan et al., 2021; Parsons & Daly, 1983; M. A. Richards &
 267 Hager, 1984). The approach we take stems from the work of Hager and O'Connell (1981)
 268 who used Green's functions to solve the equations of motion in the spherical harmonic
 269 domain. Those solutions are used to generate sensitivity kernels that straightforwardly
 270 relate, for example, density or temperature anomalies in the mantle to surface deflections.
 271 The kernels are generated in the frequency domain, and constructed such that surface
 272 deflection sensitivity to mantle (e.g., density) anomalies is calculated as a function of depth
 273 (or radius) and wavenumber. A global spherical harmonic implementation introduced
 274 by Hager et al. (1985) has been extended to include compressibility, the effect of warp-
 275 ing of the gravitational potential by subsurface density distributions, and radial grav-
 276 ity variations calculated using radial mean density values (Corrieu et al., 1995; Forte &
 277 Peltier, 1991; Hager & O'Connell, 1981; M. A. Richards & Hager, 1984; Thoraval et al.,
 278 1994).

279 In this study, following Ghelichkhan et al. (2021), surface deflection for each spher-
 280 ical harmonic coefficient, h_{lm} , is calculated in the spectral domain such that

$$h_{lm} = \frac{1}{(\rho_m - \rho_w)} \int_{R_{\text{CMB}}}^R A_l \delta \rho_{lm}(r) \cdot dr. \quad (4)$$

281 Products of the sensitivity kernel, A_l , and density anomalies, $\delta \rho_{lm}$, of spherical harmonic
 282 degree, l , and order, m , are integrated with respect to radius, r , between the core-mantle
 283 boundary and Earth's surface radii, R_{CMB} and R , respectively. The sensitivity kernel
 284 is given by

$$A_l = - \left(\frac{\eta_0}{R g_R} \right) \left(u_1 + \frac{\rho_w}{\rho_0} u_3 \right), \quad (5)$$

285 where $u_n(r)$ represents a set of poloidal variables, which are posed for solution of the set
 286 of simultaneous equations by matrix manipulation, such that

$$u(r) = [y_1 \eta_0 \quad y_2 \eta_0 \Lambda \quad (y_3 + \bar{\rho}(r)y_5)r \quad y_4 r \Lambda \quad y_5 r \rho_0 \Lambda \quad y_6 r^2 \rho_0]^T, \quad (6)$$

287 where $\Lambda = \sqrt{l(l+1)}$, and y_1 to y_6 represent the spherical harmonic coefficients of ra-
 288 dial velocity v_r , lateral velocity $v_{\theta,\phi}$, radial stress σ_{rr} , lateral stress $\sigma_{r\theta,\phi}$, gravitational
 289 potential V , and gravitational potential gradient $\partial V / \partial r$, respectively (Hager & Clayton,
 290 1989; Panasyuk et al., 1996). $\bar{\rho}$ is the layer mean ($l = 0$) density. The kernel A_l includes
 291 both u_1 and u_3 , two terms in the matrix solution to the governing equations that affect
 292 surface topography by directly exerting stress on the surface boundary (u_1), and by chang-
 293 ing the gravitational potential at the surface (u_3). The functional forms of calculated
 294 sensitivity kernels depend on chosen radial viscosity profiles and boundary conditions
 295 (e.g., free-slip or no-slip; Parsons & Daly, 1983).

296 **3 Spatial and Spectral Comparison of Model Predictions**

297 To quantify impacts of modelling assumptions and approaches used to solve the
 298 equations of motion we compare calculated surface deflections using the following met-
 299 rics.

300 **3.1 Euclidean Comparisons of Amplitudes**

301 First, we calculate root-mean-squared difference, χ , between predicted surface de-
302 flections in the spatial domain,

$$\chi = \sqrt{\frac{1}{N} \sum_{n=1}^N w_\phi (h_n^a - h_n^b)^2}, \quad (7)$$

303 where h_n^a and h_n^b are predicted surface deflections from the two models being compared.
304 N = number of points in the $1 \times 1^\circ$ gridded maps being compared (e.g., Figure 3b; $N =$
305 65341). The prefactor w_ϕ is proportional to $\cos \phi$, where ϕ is latitude, and is included
306 to correct biases in cell size with latitude; mean $w_\phi = 1$. This metric is closely asso-
307 ciated with the mean vertical distance (L^2 -norm distance) between predicted and ref-
308 erence surfaces, i.e., $\Delta \bar{h} = 1/N \sum_{n=1}^N w_\phi |h_n^a - h_n^b|$. These metrics are sensitive to dif-
309 ferences in amplitudes and locations of surface deflections.

310 **3.2 Spectral Correlation Coefficients**

311 Second, we use `pystools v4.10` to compute correlation coefficients, r_l , between pre-
312 dicted surface deflections in the spectral domain (Wieczorek & Meschede, 2018). Cor-
313 relation coefficients as a function of degree l , adapted from Forte (2007), are calculated
314 such that

$$r_l = \frac{\sum f_1^* f_2}{\sqrt{\sum f_1^* f_1} \sqrt{\sum f_2^* f_2}}, \quad \text{where } \sum = \sum_{m=-l}^{+l}, \quad (8)$$

315 f_1 and f_2 are the spherical harmonic coefficients of the two fields (i.e., surface deflections)
316 being compared, which vary as a function of order, m , and l ; $f = f_l^m$. * indicates com-
317 plex conjugation (see also Becker & Boschi, 2002; O'Connell, 1971). This metric is sen-
318 sitive to the difference between predicted and reference surface deflection signals in the
319 frequency domain, but not to their amplitudes. To summarize spectral similarity between
320 models concisely, we later refer to the mean value of r_l over every degree (0–50) as \bar{r}_l .
321 We refer to the standard deviation of r_l across degrees as s_r .

322 **3.3 Comparing Calculated Power Spectra**

323 Lastly, to estimate closeness of fit between power spectra of surface deflections pre-
324 dicted in this study and independent estimates, we calculate

$$\chi_p = \sqrt{\frac{1}{L} \sum_{l=1}^L (\log_{10} P_l - \log_{10} P_l^K)^2} + \sqrt{\frac{1}{L} \sum_{l=1}^L (\log_{10} P_l - \log_{10} P_l^H)^2}, \quad (9)$$

325 where L = number of spherical harmonic degrees being compared ($L = 50$). P_l = power
326 of predicted surface deflections generated in this study at degrees $1 \leq l \leq L$ (Equa-
327 tion 11 in Supporting Information). P_l^K = power of surface deflections estimated using
328 Kaula's law (Equation 3). P_l^H = power of residual oceanic age-depth measurements from
329 Holdt et al. (2022).

330 **4 Model Parameterizations**

331 The models examined in this paper are summarised in Table 1. In terms of assump-
332 tions tested there are two families of models, those with viscosity independent of tem-

Table 1. Summary of mantle convection simulations. Column labeled ‘Method’ indicates surface deflections calculated using either ‘*Numeric*’ (i.e., from surface normal stresses calculated using TERRA) or ‘*Analytic*’ (i.e., propagator matrix) approaches; ‘*Mixed*’ indicates spherical harmonic fitting of surface stresses calculated using numeric code, enabling comparison with solutions to propagator matrix code. $\eta(r)$ indicates models with radial viscosity (e.g. independent of temperature; Models 1–10). $\eta(r, T)$ indicates models with temperature-dependent (therefore laterally varying) viscosity (Models 11–20); note that analytic Models 12–20 incorporate radial viscosity calculated using mean radial viscosity from Model 11a. [†]indicates with respect to Model 12. See Table 1, Section 4 and figures referred to in column 5 for details.

Model	Method	Viscosity	Parameterizations	Figures
1a	Numeric	$\eta(r)$	Full resolution numeric model	1g-h, 2a-c, S1-2
1b	Mixed	$\eta(r)$	Spherical harmonic fit to 1a	2d-i
2	Analytic	$\eta(r)$	Propagator matrix solutions	3, S3
3	Analytic	$\eta(r)$	Radial gravitation, $g(r)$	4a-c, S4
4	Analytic	$\eta(r)$	Gravitational potential terms	4d-e, S5
5	Analytic	$\eta(r)$	Removing upper 50 km of mantle	5a-b, S7a-d
6	Analytic	$\eta(r)$	Removing upper 100 km of mantle	5c-d, S7e-h
7	Analytic	$\eta(r)$	Removing upper 200 km of mantle	5e-f, S7i-l
8	Analytic	$\eta(r)$	No-slip surface, free CMB	6a-d
9	Analytic	$\eta(r)$	Free surface, no-slip CMB	6e-h
10	Analytic	$\eta(r)$	No-slip surface, no-slip CMB	6i-l
11a	Numeric	$\eta(r, T)$	Full resolution numeric model	S8-S10, S12a-c
11b	Mixed	$\eta(r, T)$	Spherical harmonic fit to 11a	7, S8-10, S12d-g
12	Analytic	$\eta(r)$	Mean radial $\eta(r, T)$ from Model 11a	7, S11, S12h-k
13	Analytic	$\eta(r)$	Decrease [†] radial upper mantle η	8a-b, S13a-d
14	Analytic	$\eta(r)$	Increase [†] radial upper mantle η	8c-d, S13e-h
15	Analytic	$\eta(r)$	Increase [†] radial upper mantle η	8e-f, S13i-l
16	Analytic	$\eta(r)$	Constant radial η	8g-h, S13m-p
17	Analytic	$\eta(r)$	Upper mantle densities $\times 2^{\dagger}$	8i, S14a-c
18	Analytic	$\eta(r)$	Upper mantle densities $\times 1/2^{\dagger}$	8j, S14d-f
19	Analytic	$\eta(r)$	Lower mantle densities $\times 2^{\dagger}$	8k, S14g-i
20	Analytic	$\eta(r)$	Lower mantle densities $\times 1/2^{\dagger}$	8l, S14j-l

perature (Models 1–10), and those with temperature-dependent viscosity (Models 11–20). We note that Models 12–20 incorporate mean radial viscosity from the numeric Model 11a in which viscosity depends on temperature. The two approaches used to solve the equations of motion are annotated ‘*Numeric*’ and ‘*Analytic*’ in Table 1, which refers to solutions from the TERRA and propagator matrix code, respectively. Viscosities and densities calculated using TERRA were used as input for the propagator matrix code and thus used to generate analytic estimates of surface deflection. Since analytic solutions are obtained by spherical harmonic expansion, surface deflections from TERRA were fit using spherical harmonics before predicted deflections were compared (annotated ‘*Mixed*’ in Table 1; Section 2.2). We compare predicted deflections that arise from flow across entire model domains, i.e., from the CMB to the surface. Parameterizations of these models and resultant surface deflections are discussed in the following sections, with summary statistics given in Table 2.

346

347 **4.1 Models with Viscosity Independent of Temperature**348 **4.1.1 Reference models**

349 Models 1 and 2 are the simplest explored in this paper. They were designed to be
 350 as similar as possible, with a view to quantifying differences and similarities arising solely
 351 from the choice of numeric or analytic methodology used to solve equations of motion
 352 and to calculate surface deflections. Model 1 was parameterized with the radial viscos-
 353 ity structure shown in Figure 2c. Radial viscosity used in other geodynamic studies are
 354 shown alongside for comparison (Ghelichkhan et al., 2021; Mitrovica & Forte, 2004; Stein-
 355 berger & Calderwood, 2006). Figure 2d shows spherical harmonic expansion of the sur-
 356 face stress field predicted by Model 1 at 0 Ma (cf. Figure 2a). We call this result Model
 357 1b. The original, full-resolution, numerical result is referred to as Model 1a.

358 Model 2 is the analytic model parameterized to be as similar as possible to Model
 359 1. Its sensitivity kernel, generated assuming water loading ($\rho_w = 1030 \text{ kg/m}^3$), free-
 360 slip surface and CMB boundary conditions, and the radial viscosity profile shown in Fig-
 361 ure 2c, is shown in Figure 3a. Values of the other parameters used to generate these ker-
 362 nels are stated in Table S1. Similar to many previous studies, the kernel indicates that
 363 surface deflections will be especially sensitive (across all degrees incorporated, $l \leq 50$)
 364 to density anomalies in the upper mantle (Parsons & Daly, 1983; Hager & Clayton, 1989;
 365 Ghelichkhan et al., 2021). Models 1 and 2 are used as points of reference for other more
 366 complex models explored in the remainder of this paper.

367 **4.1.2 Gravitation**

368 We start by incorporating more complex parameterizations of gravitation. The an-
 369alytic Model 3 was parameterized in the same way as Model 2 with the addition of ra-
 370 dial gravitation (following Hager & Clayton, 1989; Panasyuk et al., 1996, see Equation
 371 5). The solid curve in Figure 4b shows the radial gravity function used to calculate sur-
 372 face deflections. It was generated using the density distribution produced by (the nu-
 373 matical) Model 1a (see Figure S1) by calculating

$$g(r) = \frac{4\pi G}{r^2} \left[\int_{R_{\text{CMB}}}^r \bar{\rho}(r') r'^2 dr' \right] + F_{\text{core}}, \quad (10)$$

374 where $\bar{\rho}(r)$ is layer mean density and F is a factor chosen to account for core mass, and
 375 such that $g = 9.8 \text{ m s}^{-2}$ at the surface. This formulation is derived from Gauss's law
 376 assuming spherically symmetric density, combined with Newton's law of universal grav-
 377 itation (Turcotte & Schubert, 2002).

378 The analytic Model 4 incorporates stress perturbations induced by deflections of
 379 the gravitational potential field. This model assumes $g = 10 \text{ m s}^{-2}$ everywhere, even
 380 within the deflected surface layer, as was the case for Models 1–2. Following Hager and
 381 Clayton (1989) and Panasyuk et al. (1996), when solving for surface deflection using prop-
 382 agator matrices, the effect on flow of perturbation of gravitational potential is included
 383 via the u_3 term in Equation 6 (see also Ribe, 2007; Ricard, 2015). Sensitivity kernels for
 384 Models 3 and 4 are shown in Figure S6. TERRA simulations do not include this com-
 385 ponent in flow calculations (see Supporting Information).

386 **4.1.3 Discarding Shallow Structure**

387 The uppermost few hundred kilometers of geodynamic simulations are often not
 388 included in predictions of surface deflections (see e.g. Flament et al., 2013; Flament, 2018;

389 Davies et al., 2019, and references therein). To quantify the impact of discarding shallow
 390 structure on our calculations, we examine differences in calculated deflections in the spatial and spherical harmonic domains. We present three tests, resulting in Models 5,
 391 6 and 7, where structure shallower than 50, 100 and 200 km is removed from Model 2.

393 4.1.4 *Changing Boundary Conditions*

394 Up to now, we have only considered instantaneous analytic and numeric solutions
 395 for surface deflection where both the surface and CMB have free-slip conditions imposed
 396 (i.e., vertical component of flow velocity $\mathbf{u}_r = 0$, horizontal components are allowed to
 397 freely vary). No gradient/Neumann constraint (e.g., on $\partial\mathbf{u}/\partial z$) is imposed. This con-
 398 dition is generally deemed appropriate for the surface of the convecting mantle, and CMB,
 399 since at both boundaries, cohesion within convecting mantle is thought to be much stronger
 400 than adhesion to the boundary. Analytic solutions for sensitivity kernels for propaga-
 401 tor matrices also exist for no-slip Dirichlet boundary conditions, where horizontal com-
 402 ponents of $\mathbf{u} = 0$, which may be more appropriate when the Earth's lithosphere is im-
 403 plicitly included in mantle convection models, as is the case here (Parsons & Daly, 1983;
 404 Thoraval & Richards, 1997). Therefore, we test the effect of changing the surface bound-
 405 ary condition to no-slip on predicted surface deflections (Model 8). Although there is lit-
 406 tle reason to believe the adhesion of the CMB would be strong, for completeness, we test
 407 scenarios in which no- and free-slip conditions are assumed for the CMB and the sur-
 408 face, respectively (Model 9), and both have no-slip conditions (Model 10).

409 4.2 Models with Temperature-Dependent Viscosity

410 We investigate the impact of including the temperature dependence of viscosity,
 411 $\eta(r, T)$, on predicted global mantle flow in numeric models, and on subsequent estimates
 412 of surface deflection. We do so by first generating the numeric Model 11, which is iden-
 413 tical to Model 1 in terms of all boundary conditions, initialization, and physical param-
 414 eters, except for the fact that viscosity depends on temperature in the manner described
 415 by Equation 7 in Supporting Information.

416 The radial distribution of viscosity, but not its absolute value, plays a crucial role
 417 in determining sensitivity of instantaneous solutions for surface deflections to density (and
 418 thermal) anomalies in the mantle (e.g., Parsons & Daly, 1983; Hager, 1984). Consequently,
 419 to assess sensitivity of surface deflections to arbitrary changes to radial viscosity, $\eta(r)$,
 420 we performed a suite of analytic tests. Since the analytic approaches require viscosity
 421 to only vary as a function of radius, we first test the impact of inserting layer-mean vis-
 422 cosity from the present-day 3D temperature-dependent viscosity structure predicted by
 423 numeric Model 11 (Figure S8). This parameterization is used to generate (the analytic)
 424 Model 12. The sensitivity kernel for Model 12 is shown in Figure S11a.

425 We stress that in Models 3–10 analytic instantaneous solutions for surface deflec-
 426 tion, with adjusted parameters and boundary conditions, were simply compared with Model
 427 2; no new numeric models were generated using TERRA. In contrast, the additional tests
 428 examined here correspond to a new TERRA model (Model 11) in which temperature de-
 429 pendence of viscosity affects mantle flow across the entire run time.

430 The sensitivity of surface deflections to arbitrary modification of upper and lower
 431 mantle viscosity and densities were then examined. Mean upper and lower mantle (ra-
 432 dial) temperature-dependent viscosity was decreased or increased by an order of mag-
 433 nitude from that used to generate Model 12 (see solid black curve in Figure 8). The re-
 434 sultant impact on calculated surface deflections (Models 13–16) was quantified by com-
 435 parison with results generated using reference Model 12 (Figure S11). Figures 8i–l and
 436 S14 show the amplitudes of density anomalies in the upper and lower mantle that were
 437 systematically increased or decreased to generate Models 17–20. Similar to the tests shown

438 in Figures 8a–h and S13, densities are amplified relative to Model 12. Radial viscosity
 439 is constant for each of these tests (black curve in Figure 8a; i.e., same as that used to
 440 generate Model 12).

441 5 Results

442 5.1 Models with Viscosity Independent of Temperature

443 5.1.1 Reference Models: Comparing Numeric and Analytic Solutions

444 We first compare solutions generated from numeric Model 1a, with its spherical har-
 445 monic representation (Model 1b), and analytic Model 2, which were designed to be as
 446 similar as possible. Figure 1g–h shows calculated densities that arise in Model 1a at 0
 447 and 100 Ma (see Figure S1 for extended results). The history of plate motions used to
 448 drive these models is also indicated on these figures. The resultant normal stresses, σ_{rr} ,
 449 calculated at the surface of Model 1, and associated statistics are shown in Figure 2a–
 450 b. By convention, positive stresses imply compression and hence downward surface de-
 451 flection, which could be manifest as lithospheric drawdown, i.e., subsidence. Prominent
 452 regions of positive stress anomalies in this model include locations atop imposed colli-
 453 sion zones, where subduction naturally results, e.g., along the Pacific margin of South
 454 America. Negative stresses imply dilation and hence positive lithospheric support (i.e.,
 455 surface uplift). Figure 2a shows dilatational stresses beneath Southern Africa, for exam-
 456 ple, and along mid-oceanic ridges in the Indian and Atlantic Oceans.

457 Surface stresses calculated by fitting radial stresses from Model 1a with a global
 458 spherical harmonic interpolation up to maximum degree $l = 50$, i.e., minimum wave-
 459 length of ≈ 800 km, is shown in Figure 2d–e. The resultant power spectrum in terms
 460 of total power at each degree is shown in Figure 2f. Aside from the lack of structure at
 461 degree 0, amplitudes decrease steadily with increasing degree (i.e., decreasing wavelength)
 462 and can be approximated by red noise. The spherical harmonic representation of deflec-
 463 tions calculated by converting stress using Equation 2, assuming water loading, are shown
 464 in Figures 2g and S2. A comparison of calculated power spectra, expected surface de-
 465 flection from Kaula’s rule (Equation 3), and spectra generated from observed residual
 466 ocean age-depth measurements is also included in Figures 2 and S2 (Kaula, 1963; Hog-
 467 gard et al., 2016; Holdt et al., 2022). For completeness, surface deflections calculated as
 468 suming air loading are shown in Figure S2f–j.

469 Surface deflections predicted by Model 2 and its associated sensitivity kernel are
 470 shown in Figure 3a–b. An expanded set of results including sensitivity kernels for wa-
 471 ter and air loading, and histograms of deflection and associate power spectra are included
 472 in Figure S3.

473 Deflections predicted from these numeric and analytic models are visually similar
 474 (cf. Figures 2g & 3b). Absolute differences in amplitudes are greatest close to subduc-
 475 tion zones (e.g., in South America and Asia; Figure 3c). The differences are broadly nor-
 476 mally distributed and centred on 0 (Figure 3d). The spherical harmonic correlation be-
 477 tween these models is high (close to 1 for all degrees; cf. Forte, 2007, Figure 3e). The
 478 ratios between surface deflection values in these predictions indicate that analytic sol-
 479 tions tend to be damped compared to numeric solutions. This result is emphasized by
 480 the histogram shown in Figure 3g. Multiplying amplitudes of deflections from the prop-
 481 agator matrix solutions by a factor of 1.1 brings them in-line with the numeric solutions.
 482 These results indicate that the propagator matrix approach dampens solutions by $\approx 10\%$.
 483 We note that power spectral slopes between Model 1b and 2 are similar (cf. Figures 2i
 484 and S3d). These and all other results are discussed in Section 6.

485 **5.1.2 Incorporating Self-Gravitation and Gravitational Potential of the
486 Deflected Surface**

487 Differences in deflections predicted by Model 2, which assumes constant $g = 10$
 488 m s^{-2} across all radii, and Model 3, which incorporates self-consistently calculated ra-
 489 dial gravitation, are shown in Figure 4a and 4c. Deviations in predicted instantaneous
 490 deflections are $\sim 10\%$ of maximum amplitudes predicted by Model 2 (see Table 2). Note
 491 that, for the viscosity structure used in these models, changing g in this way impacts sen-
 492 sitivity kernels most at low degrees $l \lesssim 10$ in the mid-mantle (see Figures 2c, 3a and
 493 S6).

494 We suggest that the broadly hemispherical differences in calculated deflections arise
 495 from three contributing factors. First, deviations in g between the two models are great-
 496 est in the mid-mantle, which, secondly, results in subtly different sensitivity kernels (see
 497 Figure S6). In general, surface deflection sensitivity to mid-mantle structure is highest
 498 at low degrees ($l = 1-3$), and is almost negligible at higher degrees compared to contrib-
 499 utions from the near-surface. Thus it seems likely that differences between these ker-
 500 nels would be manifest in low-degree (e.g. hemispherical) differences in surface deflec-
 501 tions. Third, in the final timestep, which is used to calculate deflections, there occurs
 502 a greater proportion of negative and positive deflections in the northern and southern
 503 hemispheres, respectively.

504 We note that incorporating radially varying gravitation into numeric simulations,
 505 which is not trivial, might materially impact calculated mantle flow fields and hence pre-
 506 dictions of surface deflections. Our results are consistent with the rule of thumb outlined
 507 in Section 7.02.2.5.2 of Ricard (2015), whereby magnitudes of differences incurred by in-
 508 clusion of full self-gravitation, i.e., $g(\theta, \phi, r)$, decay as a function of spherical harmonic
 509 degree, proportionately to $3/(2l + 1)$.

510 As expected, induced differences in surface displacement predictions are much lower
 511 in magnitude when gravitational potential of the deflected surface is included compared
 512 to when radial gravitation is incorporated (cf. Figure 4a and 4d). We note that they are
 513 of the same order of magnitude as the geoid height anomalies predicted by these mod-
 514 els. The mean Euclidean distance between the two predicted surfaces in Models 2 and
 515 4 is only ~ 110 m (compared to maximum amplitudes > 8 km), and the spherical har-
 516 monic correlation is very high across all degrees (see Table 2). Similar to the results for
 517 Model 3, the differences are concentrated at low spherical harmonic degree l . We stress
 518 that this test investigates the effect of the u_3 term on instantaneous solution for surface
 519 deflection (Equation 5). It cannot be ruled out from this test that inclusion of the ef-
 520 fect of gravitational potential field perturbation would result in greater differences across
 521 the entire model run time of a numeric model, although it is unlikely (Zhong et al., 2008).

522 **5.1.3 Excising Shallow Structure**

523 As expected from examination of surface deflection sensitivity kernels (e.g., Fig-
 524 ure 3a), removal of shallow structure (Models 4–6) results in significantly reduced am-
 525 plitudes of surface deflections (Figure 5). Doing so results in amplitudes of power spec-
 526 tra that more closely align with independent estimates (Figure 5b, f, j). The reduction
 527 in differences is largely due to the fact that the reference Model 2 has surface deflections
 528 that are much larger than independent estimates of dynamic topographic power across
 529 all degrees. We note that power spectral slopes for predicted surface deflection from Model
 530 2 are close to those generated from Kaula’s rule, and observed oceanic residual depths
 531 (Figures 2i, S2 and S3). Removing shallow structure steepens spectral slopes (i.e., re-
 532 duces power at high degrees) beyond those expected from theoretical considerations (Kaula’s
 533 rule) or observed from oceanic residual depths, akin to results from other work that ex-
 534 cised shallow structure (e.g., Flament et al., 2013; Moucha et al., 2008; Steinberger, 2007).
 535 This result is emphasized by calculated spectral coherence, r_l , between deflections with

536 and without shallow structure removed (cf. Figure 5b, d, f). While degree 1 and 2 structure
 537 remains coherent, coherence across degrees $\gtrsim 20$ decreases from ~ 0.9 to as low
 538 as 0.5, which are the largest discrepancies between any models examined in this study
 539 (Figure S7).

540 **5.1.4 Adjusting Boundary Conditions**

541 Figure 6a, e and i show predicted sensitivity kernels as a function of depth and de-
 542 gree, for no-slip/free-slip, free-slip/no-slip and no-slip/no-slip boundaries respectively,
 543 where the first condition is the surface slip condition, and the second the CMB slip con-
 544 dition. Differences to the sensitivity kernel for Model 2 (free-slip/free-slip; Figure 3a) are
 545 shown in panels b, f and j. Those panels, and panels c, g and k, demonstrate that when
 546 the surface boundary condition is ‘no-slip’, there is decreased sensitivity to short wave-
 547 length shallow structure, and increased sensitivity to long-wavelength (low degree) struc-
 548 ture across all depths. Figure 6d, h and l reveal that induced misfit in the spatial do-
 549 main is impacted to a greater degree than in tests of gravitation (Models 3 & 4), but not
 550 necessarily more severely than for removal of, say the upper 200 km of density structure
 551 from surface deflection calculations. Spectral correlation with Model 2 is most severely
 552 impacted when both surface and CMB boundaries are no-slip, which is probably phys-
 553 ically unrealistic (Model 7; see Table 2; Section 4.1.4).

554 **5.2 Adjusting Viscosity and Density Anomaly Amplitudes**

555 **5.2.1 Temperature-Dependent Viscosity**

556 Slices through the three-dimensional viscosity and density structure of Model 11,
 557 which incorporated temperature-dependent viscosity, are shown in Figure 1a, c and e.
 558 Density anomalies in the models parameterized with temperature-dependent viscosity
 559 are more localised (‘sharper’) than in the models with viscosity independent of temper-
 560 ature (e.g., Model 1; see Figures 7 & S8–S10). This result is unsurprising since temperature-
 561 dependent viscosity provides stronger mechanical contrasts between cooler subducting
 562 regions and surrounding asthenosphere (cf. Figure 1g–h & S9; Zhong et al., 2000). Nonethe-
 563 less, power spectra of calculated surface deflections are very similar (cf. Figure S10j &
 564 2i). This result emphasises the relatively small impact incorporating temperature-dependent
 565 viscosity has on surface deflections compared to, say, excising shallow structure.

566 Calculated power spectra from the analytic Model 12, which was generated using
 567 layer-mean (radial) viscosity from Model 11a, reinforces this view (cf. Figure S3a-d &
 568 Figure S11a-d). Similar to the results obtained for models without temperature-dependent
 569 viscosity (Figure 3), deflections calculated analytically are damped relative to numeric
 570 solutions (see Figure 7f). The best fit amplification factor to align propagator matrix
 571 and numeric solutions is 1.24 (24%). The effect is greater than that seen when compar-
 572 ing Models 1b and 2 because of increased short wavelength structure in Model 11 (see
 573 also Zhong et al., 2000). Nonetheless, spherical harmonic correlations, r_l , are > 0.75 for
 574 all degrees examined ($l \leq 50$), and > 0.85 for most degrees. Cell-to-cell differences in
 575 surface deflections are broadly normally distributed and centred on zero (Figure 7d).

576 A summary of comparisons between models with and without temperature-dependent
 577 viscosity is shown in Figure S12. Discrepancies in cell-to-cell deflections are broadly nor-
 578 mally distributed and centred on zero, clustering along the 1:1 relationship with max-
 579 imum $\chi = 1.51$ for full resolution (numeric) models (Figure S12b-c; see Table 2). Un-
 580 surprisingly, spherical harmonic fits and analytic results have tighter normal distribu-
 581 tions and lower χ values. Correlation coefficients are > 0.75 for nearly all degrees in all
 582 comparisons.

583 **5.2.2 Sensitivity to Upper/Lower Mantle Viscosity and Density Anoma-**
 584 **lies**

585 In order to explore the consequences of modified viscosity and density on calculated
 586 deflections we also systematically increased and decreased contrasts in the upper and lower
 587 mantle (Models 13–20) with respect to Model 12. Figure 8 summarises the results, which
 588 include decreasing upper mantle viscosity by an order of magnitude and show the im-
 589 pact of using increasingly simple radial viscosity in analytic calculations. Calculated sen-
 590 sitivity kernels for the adjusted viscosity profiles demonstrate that decreasing upper man-
 591 tle viscosity reduces sensitivity of surface deflections to long-wavelength density struc-
 592 ture, especially in the lower mantle (Figures S13 & 8d, f, h). Models 13–16 have broad
 593 similarities with the reference Model 12 even when $\eta(r)$ is drastically varied: average χ
 594 misfit = 0.17–0.38 km, and $r_l > 0.97$ across all degrees. These results emphasize that
 595 the viscosity adjustments we examined exert a relatively minor control on the amplitudes
 596 of instantaneous surface deflection (Table 2, see, e.g., Ghosh et al., 2010; Moucha et al.,
 597 2007; Lu et al., 2020).

598 In contrast, increasing (Model 17) or decreasing (Model 18) upper mantle densi-
 599 ties is much more impactful on amplitudes of calculated surface deflections (see Figure 8i–
 600 l, and S14). For instance, increasing or decreasing upper mantle densities by a factor of
 601 two (relative to Model 12) results in χ values of 0.97 and 0.48, respectively. Modifying
 602 lower mantle densities has a much smaller impact on amplitudes of deflection (Models
 603 18 & 19). Spherical harmonic correlation between models is approximately as good as
 604 for the radial viscosity tests (Models 13–16), which is to be expected since we do not vary
 605 locations of density anomalies here, only their amplitudes, and r_l is insensitive to am-
 606 plitudes of the two results being compared. Significant is the fact that mean vertical dif-
 607 ferences between Models 17–20 and 12 (i.e., χ and $\Delta\bar{h}$) are higher than those calculated
 608 for Models 13–16 (in which viscosity is varied; see Table 2).

609 These results emphasize the relative sensitivity of instantaneous surface deflections
 610 to upper mantle density anomalies compared to, say, radial viscosity or lower mantle den-
 611 sities. Even quite large uncertainties in lower mantle density anomalies have relatively
 612 little impact on instantaneous surface deflections. These results reinforce the view that
 613 accounting for shallow (e.g., lithospheric and asthenospheric) densities is crucial when
 614 estimating surface deflection, and dynamic topography, from mantle convection simu-
 615 lations (e.g., Colli et al., 2016; Flament et al., 2013; Holdt et al., 2022; Wang et al., 2022).

616

617 **6 Discussion**

618 **6.1 Similarities of Analytic and Numeric Solutions**

619 In this paper we compare numeric and analytic predictions of instantaneous sur-
 620 face deflections generated by mantle convection simulations. First, we simply compared
 621 predictions from numeric and analytic approaches parameterised to be as similar as pos-
 622 sible. In this test, the models were purposefully simple: viscosity is radial, models are
 623 incompressible, and they do not include self-gravitation, or radial variation in g . Numeric
 624 solutions were transformed into the frequency (spherical harmonic) domain so that they
 625 could be compared with analytic solutions, and so that power spectra could be directly
 626 compared at appropriate scales. The results show that, for as-similar-as-possible param-
 627 eterizations, amplitudes of analytic solutions are $\approx 10\%$ lower than numeric solutions
 628 (Figure 3). If the numeric model incorporates temperature-dependent viscosity, this dis-
 629 crepancy increases to 25% (Figure 7). We interpret these results in two ways. First, once
 630 armed with viscosity and density fields, numeric and analytic approaches broadly yield

Table 2. Inter-model comparison of predicted surface deflections. Models being compared are summarised in Table 1. Metrics: root-mean-squared difference (χ , km), mean Euclidean (L^2 -norm) difference in predicted deflection ($\Delta\bar{h}$, km), and mean spherical harmonic correlation between models (\bar{r}_l). Standard deviation of r_l distribution across degrees (s_r) is also stated: note that $r_l \leq 1$. All spherical harmonic representations of output from numeric code and generated by the propagator matrix code are expanded up to maximum degree, $l = 50$. See body text, figures referred to in column 6, and Table 1 for details.

Models	χ	$\Delta\bar{h}$	\bar{r}_l	s_r	Figures
1b & 2	0.95	0.69	0.97	0.02	3
2 & 3	0.57	0.47	0.99	4×10^{-4}	4
2 & 4	0.13	0.11	0.99	2×10^{-5}	4
2 & 5	0.67	0.48	0.93	0.04	5a-b
2 & 6	1.03	0.74	0.87	0.06	5c-d
2 & 7	1.57	1.12	0.63	0.15	5e-f
2 & 8	1.26	1.04	0.99	1×10^{-3}	6a-d
2 & 9	1.09	0.97	0.99	0.04	6e-h
2 & 10	1.00	0.74	0.96	0.28	6i-l
1a & 11a	1.51	1.04	—	—	S12a-c
1b & 11b	1.44	0.98	0.79	0.26	S12d-g
11b & 12	1.20	0.80	0.95	0.02	7
2 & 12	0.92	0.64	0.85	0.27	S12h-k
12 & 13	0.31	0.20	0.99	9×10^{-3}	8a-b, S13a-d
12 & 14	0.17	0.10	0.99	3×10^{-3}	8c-d, S13e-h
12 & 15	0.32	0.20	0.98	0.01	8e-f, S13i-l
12 & 16	0.38	0.23	0.98	0.01	8g-h, S13m-p
12 & 17	0.97	0.64	0.98	7×10^{-3}	8i, S14a-c
12 & 18	0.48	0.32	0.98	6×10^{-3}	8j, S14d-f
12 & 19	0.43	0.29	0.99	3×10^{-3}	8k, S14g-i
12 & 20	0.22	0.14	0.99	1×10^{-3}	8l, S14j-l

similar estimates of surface deflections. Second, the relatively damped analytic solutions are a consequence of smoothing steps in the propagator matrix approach.

The smoothness of analytic solutions, and subsequent damping of topographic amplitudes, is perhaps surprising, given the fact that they are being compared with numeric models expanded into the spherical harmonic domain to the same maximum degree, $l = 50$. However, the surface stresses used to generate Model 1a have full horizontal resolution (≈ 45 km) across depths, and *only* the surface layer is smoothed by spherical harmonic fitting, to generate Model 1b. Therefore, Model 1b inherently contains some contribution from degrees ≥ 50 , in the sense that finer-resolution density structure at depth could affect longer-wavelength flow nearer the surface. In contrast, to generate the analytic solution (Model 2), the density structure of each layer of the model is smoothed, by expansion to maximum $l = 50$, *before* integration of their contributions to surface deflection. The analytic solution would provide a better match to stress estimates from numeric models if such estimates were calculated using density structure smoothed to the same maximum l across all depths, which is currently challenging (see Section 1.1).

Nonetheless, the similarity of results indicates that the relatively low-cost propagator matrix approach can be used to explore consequences of including additional model complexity. A systematic sweep of parameters, including radial gravitation (Figure 4a-c) and gravitational potential field effects (Figure 4d-e) indicates that their effects on surface deflection are relatively modest. A useful rule of thumb is that self-gravitation perturbs instantaneous surface deflections by $O(1\text{--}10)\%$ when compared to models with constant gravitational acceleration, and even less difference is observed at high degree (e.g., Ricard, 2015, their Section 7.02.2.5.2). Incorporating the effect of deflections of gravitational potential field on flow has a modest impact on amplitudes of surface deflections at degrees 1–2, but overall it contributes even less than radial variation in g to surface deflections across the scales of interest. We note that incorporating full 3-D self-gravitation into numeric simulations is currently challenging. Nonetheless, establishing its impact on the flow field over time, and resultant impact on surface deflections, may be important future work.

6.2 Importance of Viscosity and Shallow Density Anomalies for Isolating Dynamic Support

Figure 8 demonstrates that even quite large (order of magnitude) variations in viscosity do not have much impact on instantaneous surface deflections when compared to, say, modified upper mantle density anomalies, which appears to agree with the results of Davies et al. (2019) (see also Flament, 2019; Steinberger et al., 2019). Assuming no-slip boundary conditions at Earth’s surface may be appropriate for driving near-surface (lithospheric) flow throughout the main model run time, but it less clear whether no- or free-slip boundary conditions are most appropriate for calculating instantaneous dynamic topography (see, e.g., Forte & Peltier, 1994; Thoraval & Richards, 1997). Nonetheless, all calculated sensitivity kernels in this study indicate that shallow density anomalies make significant contributions to surface topography regardless of viscosity profile or boundary conditions chosen (e.g., Figure 3a; see also Colli et al., 2016; Parsons & Daly, 1983).

It is well known that disentangling contributions to Earth’s surface topography from mantle convection, lithospheric isostasy and flexure is important but not trivial (see, e.g., Davies et al., 2019; Cao & Liu, 2021; Fernandes & Roberts, 2021; Hoggard et al., 2021; Steinberger, 2016; Stephenson et al., 2021; Zhou & Liu, 2019; Wang et al., 2022). Previous studies simulating mantle convection have addressed this issue by discarding density anomalies in radial shells shallower than specified depths before calculating surface stresses (e.g., Spasojevic & Gurnis, 2012; Flament et al., 2013; Molnar et al., 2015). Similarly, analytic approaches have isolated contributions from the convecting mantle by only

incorporating information from deep shells (e.g., Colli et al., 2018). This method has the advantage of effectively removing the effect of lithospheric cooling through time from surface deflection estimates. It also avoids the need to incorporate, say, realistic crustal or depleted lithospheric layers within the viscous flow parameterization. However, uncertain oceanic and continental lithospheric thicknesses mean that choosing appropriate cut-off depths is not simple.

Out of all the tests performed in this study, removing shallow structure resulted in the largest impact on predicted surface deflections. It modifies amplitudes of deflections, locations of uplift and subsidence, and degrees over which they are resolved, and hence modifies power spectral scalings (Table 2, Figure 5). Making quantitative predictions of dynamic topography from such an approach is fraught for at least two reasons. First, if the chosen depth is shallower than the lithosphere-asthenosphere boundary in places, plate and sub-plate contributions to topography will be entangled. Second, discarding deeper layers to ensure that all plate contribution is definitely avoided means that some contributions from asthenospheric flow will be missed. Thus, such a step is unlikely to be desirable if mantle flow models are to be used to understand, say, lithospheric vertical motions, or vice versa (see e.g., Figure 3a; Davies et al., 2019; Hoggard et al., 2016). Given the calculated sensitivity kernels, excising layers in the upper few 100 km is likely to result in predictions of surface deflections that are especially inaccurate at short wavelengths, i.e., high spherical harmonic degree. An alternative approach, which may be fruitful future work, is removal of structure based on appropriately calibrated plate models, or globally averaged age-dependent density trends (e.g., F. D. Richards et al., 2020, 2023).

6.3 Assessing ‘Effective’ Contributions to Instantaneous Deflections

The results emphasise the importance of considering sensitivities of instantaneous vertical surface deflections to the location and scale of flow in the mantle. Taking inspiration from Hager and O’Connell (1981) and Parsons and Daly (1983), we calculate the net contributions from density anomaly structure to deflections, as a function of radius, latitude and longitude across all spherical harmonic degrees considered (i.e., $l = 1$ to 50). Contributions to deflections from densities at particular radii r , across all spherical harmonic degrees and orders, for each latitude and longitude, (θ, ϕ) , are calculated such that

$$h_e(\theta, \phi, r) = \sum_{l=1}^L \sum_{m=-l}^{m=l} [Y_{lm}(\theta, \phi) \cdot \delta\rho_{lm}(r) \cdot A_l(r) \cdot \Delta r], \quad (11)$$

where Δr is the radial width of the spherical shell included in the calculation (≈ 45 km for all shells from the surface to the CMB; see Supporting Information) and Y_{lm} are spherical harmonic coefficients. Mean density anomalies, $\delta\rho_{lm}$, within each shell at each latitude and longitude, and sensitivities A_l at the top of each shell are used to calculate h_e (see Section 2.3). Contributions at specific locations to surface deflections as a function of latitude and longitude, and spherical shell depth are shown in Figure 9 for Model 12, for $1 \leq l \leq 50$. Results for lower maximum degrees are shown in Supporting Information. Panels a-d show slices through effective density in the upper (at 45, 135, 360 km) and lower mantle (1445 km). A 180° cross-section showing effective densities from the core-mantle-boundary to the surface beneath the Pacific to the Indian Ocean encompassing South America and southern Africa (the same transect as shown in Figure 1) is shown in panel e. This figure again emphasizes the contribution of density anomalies in the upper mantle to surface deflections, and the risks associated with discarding shallow structure when predicting dynamic topography.

728 **6.4 Summary and Future Work**

729 Encouragingly, although predicted instantaneous surface deflections are sensitive
 730 to different parameterizations, broadly coherent patterns emerge in all models tested.
 731 Moreover, calculated deflections are relatively insensitive to the methodologies used to
 732 solve the equations of motion. For instance, incorporation of gravitational potential of
 733 deflected surfaces, self-gravitation and viscosity anomalies each generate subtly differ-
 734 ent surface deflections. Choosing to solve the equations of motion analytically or numer-
 735 ically changes calculated deflections by < 25%, even when temperature-dependent vis-
 736 cosity is included throughout the duration of a simulation.

737 In contrast, removal of shallow structure produces much larger discrepancies be-
 738 tween predicted deflections. For instance, surface deflections calculated using the entire
 739 modelling domain (core-mantle boundary to surface) have spectral slopes consistent with
 740 those of oceanic age-depth residuals, however amplitudes are over-predicted by 1–2 or-
 741 ders of magnitude. In contrast, by not including the shallowest 200 km, calculated power
 742 spectra more closely match observed amplitudes, especially at spherical harmonic de-
 743 grees > 10 (Figure 5). However, the spectral slopes of predicted deflections are redder
 744 than for the oceanic residuals, which implies that a different approach to removing the
 745 contribution of lithospheric structure is required.

746 An obvious necessary next step for accurately predicting modern dynamic support
 747 from mantle convection simulations is to incorporate accurate information about litho-
 748 spheric structure from, for instance, tomographic models (e.g., Priestley & McKenzie,
 749 2013; F. D. Richards et al., 2020). Another useful next step is to establish sensitivity of
 750 surface deflections to time-dependent parameters that impact predicted flow histories,
 751 including plate motions. The results in this paper indicate that comparing predicted and
 752 observed surface deflections, combined with knowledge of lithospheric structure, could
 753 be used to identify optimal models.

754 Finally, the body of geologic and geomorphologic observations that could be used
 755 to test predicted histories of surface deflections from mantle convection simulations has
 756 grown substantially in the last decade (e.g., uplift and subsidence histories; Section 1;
 757 see, e.g., Hoggard et al., 2021, and references therein). A suite of other geologic and geo-
 758 physical observables are also predicted by, or can be derived from, such simulations (e.g.,
 759 mantle temperatures, heat flux, geoid, seismic velocities, true polar wander). Using them
 760 alongside histories of surface deflections to identify optimal simulations is an obvious av-
 761 enue for future work (e.g., Ball et al., 2021; Lau et al., 2017; Panton et al., 2023; F. D. Richards
 762 et al., 2023). Using such data and the methodologies explored in this paper may be a
 763 fruitful way of identifying optimal simulations from the considerable inventory that al-
 764 ready exists.

765 **7 Conclusions**

766 This study is concerned with quantifying sensitivities and uncertainties of Earth's
 767 surface deflections that arise in simulations of mantle convection. Calculated sensitiv-
 768 ities of instantaneous deflection of Earth's surface to mantle density structure empha-
 769 sise the importance of accurate mapping of the upper mantle. Surface deflections are some-
 770 what sensitive to the distribution of viscosity throughout the mantle, but especially to
 771 the locations and scales of density anomalies in the upper mantle. The largest discrep-
 772 ancies between predicted deflections seen in this study are generated when upper man-
 773 tle structure is excised or altered. Doing so changes both the amplitude and distribu-
 774 tion of calculated deflections, modifying their power spectral slopes. These results em-
 775 phasise the importance of incorporating accurate models of lithospheric structure into
 776 calculation of sub-plate support of topography, and also the need to accurately deter-
 777 mine plate contributions to topography. In contrast, the choice of methodology to es-

timate surface deflections—analytic or numeric—or boundary conditions are relatively small sources of uncertainty. Similarly, assumed gravitational profiles and temperature dependence of viscosity are relatively minor contributors to uncertainty given reasonable, Earth-like, parameterizations. Nonetheless, these parameterizations may impact surface deflections through their role in determining how upper mantle flow evolves through geologic time. A fruitful next step could be to use the approaches developed in this paper, in combination with careful isolation of plate cooling signatures from surface deflection predictions, to test mantle convection simulations using the existing and growing body of geologic, geomorphologic and geophysical observations.

Open Research Section

TERRA models are archived [here]. The propagator matrix code is archived [here]. Parameterization files are archived [here]. [TO ED: this section will be completed upon final submission, when confirmation of the precise models published is obtained after review.]

Acknowledgments

We thank A. Biggin, H. Brown, C. Davies, A. Ferreira, M. Holdt, P. Japsen, P. Koelemeijer, F. McNab, R. Myhill and J. Ward for helpful discussion. We also thank N. Flament and an anonymous reviewer for helping us to clarify our thesis. C.O., J.P. and V.M.F. were supported by NERC Grant NE/T01684/1.

References

- Al-Hajri, Y., White, N., & Fishwick, S. (2009). Scales of transient convective support beneath Africa. *Geology*, 37(10), 883–886. doi: 10.1130/G25703A.1
- Bahadori, A., Holt, W., & Feng, R. e. a. (2022). Coupled influence of tectonics, climate, and surface processes on landscape evolution in southwestern North America. *Nat Commun*, 13(4437). doi: 10.1038/s41467-022-31903-2
- Ball, P. W., Duvernay, T., & Davies, D. R. (2022). A coupled geochemical-geodynamic approach for predicting mantle melting in space and time. *Geochemistry, Geophysics, Geosystems*, 23, 1–31. doi: 10.1029/2022gc010421
- Ball, P. W., White, N. J., Maclennan, J., & Stephenson, S. N. (2021). Global Influence of Mantle Temperature and Plate Thickness on Intraplate Volcanism. *Nature Communications*, 12(2045), 1–13. doi: 10.1038/s41467-021-22323-9
- Bangerth, W., Dannberg, J., Fraters, M., Gassmoeller, R., Glerum, A., Heister, T., ... Naliboff, J. (2023). ASPECT v2.5.0 [Computer software manual]. Retrieved 2023-08-04, from <https://zenodo.org/record/3924604> doi: 10.5281/zenodo.8200213
- Bauer, S., Huber, M., Ghelichkhan, S., Mohr, M., Rüde, U., & Wohlmuth, B. (2019). Large-scale simulation of mantle convection based on a new matrix-free approach. *Journal of Computational Science*, 31, 60–76. Retrieved from <https://doi.org/10.1016/j.jocs.2018.12.006> doi: 10.1016/j.jocs.2018.12.006
- Baumgardner, J. R. (1985). Three-dimensional treatment of convective flow in the Earth's mantle. *Journal of Statistical Physics*, 39(5-6), 501–511. doi: 10.1007/BF01008348
- Becker, T. W., & Boschi, L. (2002). A comparison of tomographic and geodynamic mantle models. *Geochemistry, Geophysics, Geosystems*, 3(1), 1–48. doi: 10.1029/2001GC000168
- Biggin, A. J., Steinberger, B., Aubert, J., Sutcliffe, N., Holme, R., Torsvik, T. H., ... Van Hinsbergen, D. J. (2012). Possible links between long-term geomagnetic variations and whole-mantle convection processes. *Nature Geoscience*, 5(8),

- 526–533. doi: 10.1038/ngeo1521
- Braun, J. (2010). The many surface expressions of mantle dynamics. *Nature Geoscience*, 3(12), 825–833. doi: 10.1038/ngeo1020
- Bunge, H.-P., & Baumgardner, J. R. (1995). Mantle convection modeling on parallel virtual machines. *Computers in Physics*, 9(2), 207–215. doi: 10.1063/1.168525
- Bunge, H.-P., Hagelberg, C. R., & Travis, B. J. (2003). Mantle circulation models with variational data assimilation: inferring past mantle flow and structure from plate motion histories and seismic tomography. *Geophysical Journal International*, 152, 280–301. doi: 10.1046/j.1365-246X.2003.01823
- Bunge, H.-P., Richards, M. A., & Baumgardner, J. R. (2002). Mantle-circulation models with sequential data assimilation: Inferring present-day mantle structure from plate-motion histories. *Philosophical Transactions of the Royal Society A: Mathematical, Physical and Engineering Sciences*, 360(1800), 2545–2567. doi: 10.1098/rsta.2002.1080
- Cao, Z., & Liu, L. (2021). Origin of Three-Dimensional Crustal Stress Over the Conterminous United States. *Journal of Geophysical Research: Solid Earth*, 126(11), e2021JB022137. (e2021JB022137 2021JB022137) doi: <https://doi.org/10.1029/2021JB022137>
- Chang, C., & Liu, L. (2021). Investigating the formation of the Cretaceous Western Interior Seaway using landscape evolution simulations. *GSA Bulletin*, 133(1-2), 347–361. doi: 10.1130/B35653.1
- Colli, L., Ghelichkhan, S., & Bunge, H.-P. (2016). On the ratio of dynamic topography and gravity anomalies in a dynamic Earth. *Geophysical Research Letters*, 43, 2510–2516. doi: 10.1002/2016GL067929
- Colli, L., Ghelichkhan, S., Bunge, H.-P., & Oeser, J. (2018). Retrodictions of Mid Paleogene mantle flow and dynamic topography in the Atlantic region from compressible high resolution adjoint mantle convection models: Sensitivity to deep mantle viscosity and tomographic input model. *Gondwana Research*, 53, 252–272. doi: 10.1016/j.gr.2017.04.027
- Corrieu, V., Thoraval, C., & Ricard, Y. (1995). Mantle dynamics and geoid Green functions. *Geophysical Journal International*, 120(2), 516–523. doi: 10.1111/j.1365-246X.1995.tb01835.x
- Craig, C. H., & McKenzie, D. (1987). Surface deformation, gravity and the geoid from a three-dimensional convection model at low Rayleigh numbers. *Earth and Planetary Science Letters*, 83, 123–136. doi: 10.1016/0012-821X(87)90056-2
- Cramer, F., Schmeling, H., Golabek, G. J., Duretz, T., Orendt, R., Buiter, S. J., ... Tackley, P. J. (2012). A comparison of numerical surface topography calculations in geodynamic modelling: An evaluation of the ‘sticky air’ method. *Geophysical Journal International*, 189(1), 38–54. doi: 10.1111/j.1365-246X.2012.05388.x
- Czarnota, K., Hoggard, M. J., White, N., & Winterbourne, J. (2013). Spatial and temporal patterns of Cenozoic dynamic topography around Australia. *Geochemistry, Geophysics, Geosystems*, 14(3), 634–658. doi: 10.1029/2012GC004392
- Dannberg, J., Eilon, Z., Faul, U., Gassmöller, R., Moulik, P., & Myhill, R. (2017). The importance of grain size to mantle dynamics and seismological observations. *Geochemistry, Geophysics, Geosystems*, 18(8), 3034–3061. doi: 10.1002/2017GC006944
- Davies, D. R., Davies, J. H., Bollada, P. C., Hassan, O., Morgan, K., & Nithiarasu, P. (2013). A hierarchical mesh refinement technique for global 3-D spherical mantle convection modelling. *Geoscientific Model Development*, 6(4), 1095–1107. doi: 10.5194/gmd-6-1095-2013
- Davies, D. R., Ghelichkhan, S., Hoggard, M. J., Valentine, A. P., & Richards, F. D.

- 882 (2023). Observations and Models of Dynamic Topography: Current Status and
 883 Future Directions. In J. Duarte (Ed.), *Dynamics of plate tectonics and mantle*
 884 *convection* (pp. 223–269). Elsevier. doi: 10.1016/B978-0-323-85733-8.00017-2
- 885 Davies, D. R., Valentine, A. P., Kramer, S. C., Rawlinson, N., Hoggard, M. J.,
 886 Eakin, C. M., & Wilson, C. R. (2019). Earth's multi-scale topographic
 887 response to global mantle flow. *Nature Geoscience*, 12, 845–850. doi:
 888 10.1038/s41561-019-0441-4
- 889 Fernandes, V. M., & Roberts, G. G. (2021). Cretaceous to Recent net continental
 890 uplift from paleobiological data: Insights into sub-plate support. *GSA Bulletin*,
 891 133, 1–20. doi: 10.1130/b35739.1
- 892 Fernandes, V. M., Roberts, G. G., White, N., & Whittaker, A. C. (2019).
 893 Continental-Scale Landscape Evolution: A History of North American To-
 894 polography. *Journal of Geophysical Research: Earth Surface*, 124, 1–34. doi:
 895 10.1029/2018jf004979
- 896 Fichtner, A., Kennett, B. L. N., Igel, H., & Bunge, H.-P. (2009). Full seismic wave-
 897 form tomography for upper-mantle structure in the Australasian region using
 898 adjoint methods. *Geophysical Journal International*, 179(3), 1703–1725. doi:
 899 10.1111/j.1365-246X.2009.04368.x
- 900 Fichtner, A., Trampert, J., Cupillard, P., Saygin, E., Taymaz, T., Capdeville, Y., &
 901 Villaseñor, A. (2013). Multiscale full waveform inversion. *Geophysical Journal*
 902 *International*, 194, 534–556. doi: 10.1093/gji/ggt118
- 903 Fichtner, A., & Villaseñor, A. (2015). Crust and upper mantle of the western
 904 Mediterranean - Constraints from full-waveform inversion. *Earth and Plane-*
 905 *tary Science Letters*, 428, 52–62. doi: 10.1016/j.epsl.2015.07.038
- 906 Flament, N. (2018). Present-day dynamic topography and lower-mantle structure
 907 from palaeogeographically constrained mantle flow models. *Geophysical Jour-*
 908 *nal International*, 216(3), 2158–2182. doi: 10.1093/gji/ggy526
- 909 Flament, N. (2019). Present-day dynamic topography and lower-mantle structure
 910 from palaeogeographically constrained mantle flow models. *Geophysical Jour-*
 911 *nal International*, 216(3), 2158–2182. doi: 10.1093/gji/ggy526
- 912 Flament, N., Gurnis, M., & Muller, R. D. (2013). A review of observations and mod-
 913 els of dynamic topography. *Lithosphere*, 5(2), 189–210. doi: 10.1130/L245.1
- 914 Flament, N., Gurnis, M., Müller, R. D., Bower, D. J., & Husson, L. (2015). Influ-
 915 ence of subduction history on South American topography. *Earth and Plane-*
 916 *tary Science Letters*, 430, 9–18. doi: 10.1016/j.epsl.2015.08.006
- 917 Foley, S. F., & Fischer, T. P. (2017). An essential role for continental rifts and litho-
 918 sphere in the deep carbon cycle. *Nature Geoscience*, 10(12), 897–902. doi: 10
 919 .1038/s41561-017-0002-7
- 920 Forte, A. M. (2007). Constraints on Seismic Models from Other Disciplines -
 921 Implications for Mantle Dynamics and Composition. In B. Romanowicz &
 922 A. Dziewonski (Eds.), *Seismology and the structure of the earth* (pp. 805–858).
 923 Elsevier B.V. doi: 10.1016/B978-044452748-6.00027-4
- 924 Forte, A. M., & Peltier, R. (1991). Viscous Flow Models of Global Geophysical
 925 Observables 1. Forward Problems. *Journal of Geophysical Research*, 96(B12),
 926 20131–20159. doi: 10.1029/91JB01709
- 927 Forte, A. M., & Peltier, W. R. (1994). The Kinematics and Dynamics of Poloidal-
 928 Toroidal Coupling in Mantle Flow: The Importance of Surface Plates and
 929 Lateral Viscosity Variations. *Advances in Geophysics*, 36, 1–119. doi:
 930 10.1016/S0065-2687(08)60537-3
- 931 French, S. W., & Romanowicz, B. (2015). Broad plumes rooted at the base of the
 932 Earth's mantle beneath major hotspots. *Nature*, 525(7567), 95–99. doi: 10
 933 .1038/nature14876
- 934 Galloway, W. E., Whiteaker, T. L., & Ganey-Curry, P. (2011). History of Ceno-
 935 zoic North American drainage basin evolution, sediment yield, and accu-
 936 mulation in the Gulf of Mexico basin. *Geosphere*, 7(4), 938–973. doi:

- 937 10.1130/GES00647.1
- 938 Gantmacher, F. R. (1959). *The Theory of Matrices*. New York: Chelsea Publishing
939 Company.
- 940 Ghelichkhan, S., Bunge, H.-P., & Oeser, J. (2021). Global mantle flow retrod-
941 ictions for the early Cenozoic using an adjoint method: Evolving dynamic
942 topographies, deep mantle structures, flow trajectories and sublithospheric
943 stresses. *Geophysical Journal International*, 226(2), 1432–1460. doi:
944 10.1093/gji/ggab108
- 945 Ghosh, A., Becker, T. W., & Zhong, S. J. (2010). Effects of lateral viscosity vari-
946 ations on the geoid. *Geophysical Research Letters*, 37(1), 2–7. doi: 10.1029/
947 2009GL040426
- 948 Ghosh, A., & Holt, W. E. (2012). Plate Motions and Stresses from Global Dynamic
949 Models. *Science*, 335(6070), 838–843. doi: 10.1126/science.1214209
- 950 Glišović, P., & Forte, A. M. (2016). A new back-and-forth iterative method for
951 time-reversed convection modeling: Implications for the Cenozoic evolution of
952 3-D structure and dynamics of the mantle. *Journal of Geophysical Research: Solid Earth*, 121(6), 4067–4084. doi: 10.1002/2016JB012841
- 953 Gunnell, Y., & Burke, K. (2008). The African Erosion Surface: A Continental-Scale
954 Synthesis of Geomorphology, Tectonics, and Environmental Change over the
955 Past 180 Million Years. *Memoir of the Geological Society of America*, 201,
956 1–66. doi: 10.1130/2008.1201
- 957 Gurnis, M., Mitrovica, J. X., Ritsema, J., & Van Heijst, H.-J. (2000). Constraining
958 mantle density structure using geological evidence of surface uplift rates: The
959 case of the African Superplume. *Geochemistry, Geophysics, Geosystems*, 1(7),
960 1–35. doi: 10.1029/1999GC000035
- 961 Hager, B. H. (1984). Subducted Slabs and the Geoid: Constraints on Mantle Rheol-
962 ogy and Flow. *Journal of Geophysical Research*, 89(B7), 6003–6015.
- 963 Hager, B. H., & Clayton, R. W. (1989). Constraints on the Structure of Man-
964 tle Convection Using Seismic Observations, Flow Models, and the Geoid. In
965 W. R. Peltier (Ed.), *Mantle convection: Plate tectonics and global dynamics*
966 (pp. 657–763). New York: Gordon and Breach Science Publishers.
- 967 Hager, B. H., Clayton, R. W., Richards, M. A., Comer, R. P., & Dziewonski, A. M.
968 (1985). Lower mantle heterogeneity, dynamic topography and the geoid. *Nature*,
969 313, 541–545. doi: 10.1038/314752a0
- 970 Hager, B. H., & O'Connell, R. J. (1979). Kinematic Models of Large-Scale Flow in
971 the Earth's Mantle. *Journal of Geophysical Research*, 84(B3), 1031–1048.
- 972 Hager, B. H., & O'Connell, R. J. (1981). A Simple Global Model of Plate Dynamics
973 and Mantle Convection. *Journal of Geophysical Research*, 86(B6), 4843–4867.
974 doi: 10.1029/JB086iB06p04843
- 975 Hazzard, J. A. N., Richards, F. D., Goes, S. D. B., & Roberts, G. G. (2022). Prob-
976 abilistic Assessment of Antarctic Thermomechanical Structure: Impacts on Ice
977 Sheet Stability. *EarthArXiv*. doi: 10.31223/X5C35R
- 978 Heister, T., Dannberg, J., Gassmöller, R., & Bangerth, W. (2017). High accuracy
979 mantle convection simulation through modern numerical methods – II: realistic
980 models and problems. *Geophysical Journal International*, 210(2), 833–851.
981 doi: 10.1093/gji/ggx195
- 982 Hoggard, M. J., Austermann, J., Randel, C., & Stephenson, S. (2021). Observa-
983 tional Estimates of Dynamic Topography Through Space and Time. In *Mantle
984 convection and surface expressions* (pp. 371–411). AGU. doi: 10.1002/
985 9781119528609.ch15
- 986 Hoggard, M. J., White, N., & Al-Attar, D. (2016). Global dynamic topography
987 observations reveal limited influence of large-scale mantle flow. *Nature Geo-
988 science*, 9(May), 1–8. doi: 10.1038/ngeo2709
- 989 Holdt, M. C., White, N. J., Stephenson, S. N., & Conway-Jones, B. W. (2022).
990 Densely Sampled Global Dynamic Topographic Observations and Their Signifi-
991

- cance. *Journal of Geophysical Research: Solid Earth*, *127*, 1–32.
- 992
993 Jeans, J. H. (1923). The Propagation of Earthquake Waves. *Proceedings of the Royal*
994 *Society of London A*, *102*(718), 554–574.
- 995 Kaula, W. M. (1963). Determination of the Earth's Gravitational Field. *Reviews of*
996 *Geophysics*, *1*(4), 507–551.
- 997 Kramer, S. C., Davies, D. R., & Wilson, C. R. (2021). Analytical solutions for man-
998 tle flow in cylindrical and spherical shells. *Geoscientific Model Development*,
999 *14*(4), 1899–1919. doi: 10.5194/gmd-14-1899-2021
- 1000 Lambeck, K., Smither, C., & Johnston, P. (1998). Sea-level change, glacial rebound
1001 and mantle viscosity for northern Europe. *Geophysical Journal International*,
1002 *134*, 102–144. doi: 10.1046/j.1365-246X.1998.00541.x
- 1003 Lau, H. C. P., Mitrovica, J. X., Davis, J. L., Tromp, J., Yang, H.-Y., & Al-Attar, D.
1004 (2017). Tidal tomography constrains Earth's deep-mantle buoyancy. *Nature*,
1005 *551*(7680), 321–326. doi: 10.1038/nature24452
- 1006 Lees, M. E., Rudge, J. F., & McKenzie, D. (2020). Gravity, topography, and melt
1007 generation rates from simple 3D models of mantle convection. *Geochemistry,*
1008 *Geophysics, Geosystems*, *21*, 1–29. doi: 10.1029/2019gc008809
- 1009 Lekić, V., & Fischer, K. M. (2014). Contrasting lithospheric signatures across the
1010 western United States revealed by Sp receiver functions. *Earth and Planetary*
1011 *Science Letters*, *402*, 90–98. doi: 10.1016/j.epsl.2013.11.026
- 1012 Liu, L., & Gurnis, M. (2008). Simultaneous inversion of mantle properties and initial
1013 conditions using an adjoint of mantle convection. *Journal of Geophysical Re-*
1014 *search: Solid Earth*, *113*(B8), 1–17. doi: 10.1029/2008jb005594
- 1015 Lu, C., Forte, A. M., Simmons, N. A., Grand, S. P., Kajan, M. N., Lai, H., & Gar-
1016 nero, E. J. (2020). The Sensitivity of Joint Inversions of Seismic and Geo-
1017 dynamic Data to Mantle Viscosity. *Geochemistry, Geophysics, Geosystems*,
1018 *21*(4), 1–29. doi: 10.1029/2019gc008648
- 1019 McKenzie, D. (1977). Surface deformation, gravity anomalies and convection. *Geo-*
1020 *physical Journal of the Royal Astronomical Society*, *48*, 211–238. doi: 10.1111/
1021 j.1365-246X.1977.tb01297.x
- 1022 Meredith, A. S., Williams, S. E., Collins, A. S., Tetley, M. G., Mulder, J. A., Blades,
1023 M. L., ... Müller, R. D. (2021). Extending full-plate tectonic models into deep
1024 time: Linking the Neoproterozoic and the Phanerozoic. *Earth-Science Reviews*,
1025 *214*(103477), 1–44. doi: 10.1016/j.earscirev.2020.103477
- 1026 Mitrovica, J. X., & Forte, A. M. (2004). A new inference of mantle viscosity based
1027 upon joint inversion of convection and glacial isostatic adjustment data. *Earth*
1028 *and Planetary Science Letters*, *225*(1-2), 177–189. doi: 10.1016/j.epsl.2004.06
1029 .005
- 1030 Molnar, P., England, P. C., & Jones, C. H. (2015). Mantle dynamics, isostasy, and
1031 the support of high terrain. *Journal of Geophysical Research: Solid Earth*,
1032 *120*(3), 1932–1957. doi: 10.1002/2014JB011724
- 1033 Morris, M., Fernandes, V. M., & Roberts, G. G. (2020). Extricating dynamic to-
1034 polography from subsidence patterns: Examples from Eastern North America's
1035 passive margin. *Earth and Planetary Science Letters*, *530*(115840), 1–13. doi:
1036 10.1016/j.epsl.2019.115840
- 1037 Mouha, R., & Forte, A. M. (2011). Changes in African topography driven by man-
1038 tle convection: supplementary information. *Nature Geoscience*, *4*(10), 707–712.
1039 doi: 10.1038/ngeo1235
- 1040 Mouha, R., Forte, A. M., Mitrovica, J. X., & Daradich, A. (2007). Lateral vari-
1041 ations in mantle rheology: Implications for convection related surface observ-
1042 ables and inferred viscosity models. *Geophysical Journal International*, *169*(1),
1043 113–135. doi: 10.1111/j.1365-246X.2006.03225.x
- 1044 Mouha, R., Forte, A. M., Mitrovica, J. X., Rowley, D. B., Quéré, S., Simmons,
1045 N. A., & Grand, S. P. (2008). Dynamic topography and long-term sea-level
1046 variations: There is no such thing as a stable continental platform. *Earth and*

- 1047 *Planetary Science Letters*, 271(1-4), 101–108. doi: 10.1016/j.epsl.2008.03.056
- 1048 O'Connell, R. J. (1971). Pleistocene Glaciation and the Viscosity of the Lower
- 1049 Mantle. *Geophysical Journal of the Royal Astronomical Society*, 23(3), 299–
- 1050 327. doi: 10.1111/j.1365-246X.1971.tb01823.x
- 1051 O'Malley, C. P. B., White, N. J., Stephenson, S. N., & Roberts, G. G. (2021).
- 1052 Large-Scale Tectonic Forcing of the African Landscape. *Journal of Geophysical*
- 1053 Research: Earth Surface, 126, 1–37. doi: 10.1029/2021jf006345
- 1054 Panasyuk, S. V., Hager, B. H., & Forte, A. M. (1996). Understanding the effects
- 1055 of mantle compressibility on geoid kernels. *Geophysical Journal International*,
- 1056 124(1), 121–133. doi: 10.1111/j.1365-246X.1996.tb06357.x
- 1057 Panton, J., Davies, J. H., & Myhill, R. (2023). The Stability of Dense Oceanic
- 1058 Crust Near the Core-Mantle Boundary. *Journal of Geophysical Research: Solid*
- 1059 *Earth*, 128, 1–21. doi: 10.1029/2022JB025610
- 1060 Parsons, B., & Daly, S. (1983). The relationship between surface topography, gravity
- 1061 anomalies and temperature structure of convection. *Journal of Geophysical Re-*
- 1062 *search*, 88(B2), 1129–1144. doi: 10.1029/JB088iB02p01129
- 1063 Pekeris, C. L. (1935). Thermal Convection in the Interior of the Earth. *Geophysical*
- 1064 *Supplements to the Monthly Notices of the Royal Astronomical Society*, 3(8),
- 1065 343–367.
- 1066 Priestley, K., & McKenzie, D. (2013). The relationship between shear wave
- 1067 velocity, temperature, attenuation and viscosity in the shallow part of
- 1068 the mantle. *Earth and Planetary Science Letters*, 381, 78–91. doi:
- 1069 10.1016/j.epsl.2013.08.022
- 1070 Ribe, N. M. (2007). Analytical Approaches to Mantle Dynamics. *Treatise on Geo-*
- 1071 *physics*, 7, 167–226. doi: 10.1016/B978-044452748-6.00117-6
- 1072 Ricard, Y. (2007). Physics of Mantle Convection. *Treatise on Geophysics*, 7, 31–88.
- 1073 Ricard, Y. (2015). Physics of Mantle Convection. In G. Schubert (Ed.), *Treatise on*
- 1074 *geophysics* (pp. 23–71). doi: 10.1016/B978-044452748-6.00115-2
- 1075 Richards, F. D., Hoggard, M. J., Ghelichkhan, S., Koelemeijer, P., & Lau, H. C. P.
- 1076 (2021). Geodynamic, geodetic, and seismic constraints favour deflated and
- 1077 dense-cored LLVPs. *EarthArXiv*, 1–20. doi: 10.31223/X55601
- 1078 Richards, F. D., Hoggard, M. J., Ghelichkhan, S., Koelemeijer, P., & Lau, H. C. P.
- 1079 (2023). Geodynamic, geodetic, and seismic constraints favour deflated and
- 1080 dense-cored LLVPs. *Earth and Planetary Science Letters*, 602(117964), 1–13.
- 1081 doi: 10.1016/j.epsl.2022.117964
- 1082 Richards, F. D., Hoggard, M. J., White, N., & Ghelichkhan, S. (2020). Quantifying
- 1083 the relationship between short-wavelength dynamic topography and thermo-
- 1084 mechanical structure of the upper mantle using calibrated parameterization
- 1085 of anelasticity. *Journal of Geophysical Research: Solid Earth*, 125, 1–36. doi:
- 1086 10.1029/2019JB019062
- 1087 Richards, M. A., & Hager, B. H. (1984). Geoid Anomalies in a Dynamic
- 1088 Earth. *Journal of Geophysical Research*, 89(B7), 5987–6002. doi: 10.1029/
- 1089 JB089iB07p05987
- 1090 Salles, T., Flament, N., & Müller, D. (2017, jan). Influence of mantle flow on the
- 1091 drainage of eastern Australia since the Jurassic Period. *Geochemistry, Geo-*
- 1092 *physics, Geosystems*, 18(1), 280–305. doi: 10.1002/2016GC006617
- 1093 Spasojevic, S., & Gurnis, M. (2012). Sea level and vertical motion of continents from
- 1094 dynamic earth models since the Late Cretaceous. *AAPG Bulletin*, 96(11),
- 1095 2037–2064. doi: 10.1306/03261211121
- 1096 Stanley, J. R., Braun, J., Baby, G., Guillocheau, F., Robin, C., Flowers, R. M.,
- 1097 ... Beucher, R. (2021). Constraining Plateau Uplift in Southern Africa by
- 1098 Combining Thermochronology, Sediment Flux, Topography, and Landscape
- 1099 Evolution Modeling. *Journal of Geophysical Research: Solid Earth*, 126, 1–34.
- 1100 doi: 10.1029/2020JB021243
- 1101 Steinberger, B. (2007). Effects of latent heat release at phase boundaries on flow in

- the Earth's mantle, phase boundary topography and dynamic topography at the Earth's surface. *Physics of the Earth and Planetary Interiors*, 164(1-2), 2–20. doi: 10.1016/j.pepi.2007.04.021
- Steinberger, B. (2016). Topography caused by mantle density variations: Observation-based estimates and models derived from tomography and lithosphere thickness. *Geophysical Journal International*, 205(1), 604–621. doi: 10.1093/gji/ggw040
- Steinberger, B., & Antretter, M. (2006). Conduit diameter and buoyant rising speed of mantle plumes: Implications for the motion of hot spots and shape of plume conduits. *Geochemistry, Geophysics, Geosystems*, 7(11), 1–25. doi: 10.1029/2006GC001409
- Steinberger, B., & Calderwood, A. R. (2006). Models of large-scale viscous flow in the Earth's mantle with constraints from mineral physics and surface observations. *Geophysical Journal International*, 167(3), 1461–1481. doi: 10.1111/j.1365-246X.2006.03131.x
- Steinberger, B., Nelson, P. L., Grand, S. P., & Wang, W. (2019). Yellowstone plume conduit tilt caused by large-scale mantle flow. *Geochemistry, Geophysics, Geosystems*, 20, 5896–5912. doi: 10.1029/2019gc008490
- Stephenson, S. N., White, N. J., Carter, A., Seward, D., Ball, P. W., & Klöcking, M. (2021). Cenozoic Dynamic Topography of Madagascar. *Geochemistry, Geophysics, Geosystems*, 22, 1–38. doi: 10.1029/2020gc009624
- Tackley, P. J., Stevenson, D. J., Glatzmaier, G. A., & Schubert, G. (1993). Effects of an endothermic phase transition at 670 km depth on spherical mantle convection. *Nature*, 361, 699–704. doi: 10.1038/361699a0
- Thoraval, C., Machete, P., & Cazenave, A. (1994). Influence of mantle compressibility and ocean warping on dynamical models of the geoid. *Geophysical Journal International*, 117, 566–573. doi: 10.1111/j.1365-246X.1994.tb03954.x
- Thoraval, C., & Richards, M. A. (1997). The geoid constraint in global geodynamics: Viscosity structure, mantle heterogeneity models and boundary conditions. *Geophysical Journal International*, 131, 1–8. doi: 10.1111/j.1365-246X.1997.tb00591.x
- Topographic asymmetry of the south atlantic from global models of mantle flow and lithospheric stretching. (2014). *Earth and Planetary Science Letters*, 387, 107–119. doi: 10.1016/j.epsl.2013.11.017
- Turcotte, D. L., & Schubert, G. (2002). *Geodynamics* (Second Edi ed.). Cambridge University Press.
- Wang, Y., Liu, L., & Zhou, Q. (2022). Topography and gravity reveal denser cratonic lithospheric mantle than previously thought. *Geophysical Research Letters*, 49(1). doi: <https://doi.org/10.1029/2021GL096844>
- Wieczorek, M. A., & Meschede, M. (2018). SHTools: Tools for Working with Spherical Harmonics. *Geochemistry, Geophysics, Geosystems*, 19, 1–19. doi: 10.1029/2018GC007529
- Zhong, S., Gurnis, M., & Hulbert, G. (1993). Accurate determination of surface normal stress in viscous flow from a consistent boundary flux method. *Physics of the Earth and Planetary Interiors*, 78, 1–8. doi: 10.1016/0031-9201(93)90078-N
- Zhong, S., McNamara, A., Tan, E., Moresi, L., & Gurnis, M. (2008). A benchmark study on mantle convection in a 3-D spherical shell using CitcomS. *Geochemistry, Geophysics, Geosystems*, 9(10), 1–32. doi: 10.1029/2008GC002048
- Zhong, S., Zuber, M. T., Moresi, L., & Gurnis, M. (2000). Role of temperature-dependent viscosity and surface plates in spherical shell models of mantle convection. *Journal of Geophysical Research*, 105(B5), 11063–11082.
- Zhou, Q., & Liu, L. (2019). Topographic evolution of the western United States since the early Miocene. *Earth and Planetary Science Letters*, 514, 1–12. doi: 10.1016/j.epsl.2019.02.029

- 1157 Zhou, Q., Liu, L., & Hu, J. (2018). Western US volcanism due to intruding oceanic
1158 mantle driven by ancient Farallon slabs. *Nature Geoscience*, 11, 70–76. doi: 10
1159 .1038/s41561-017-0035-y

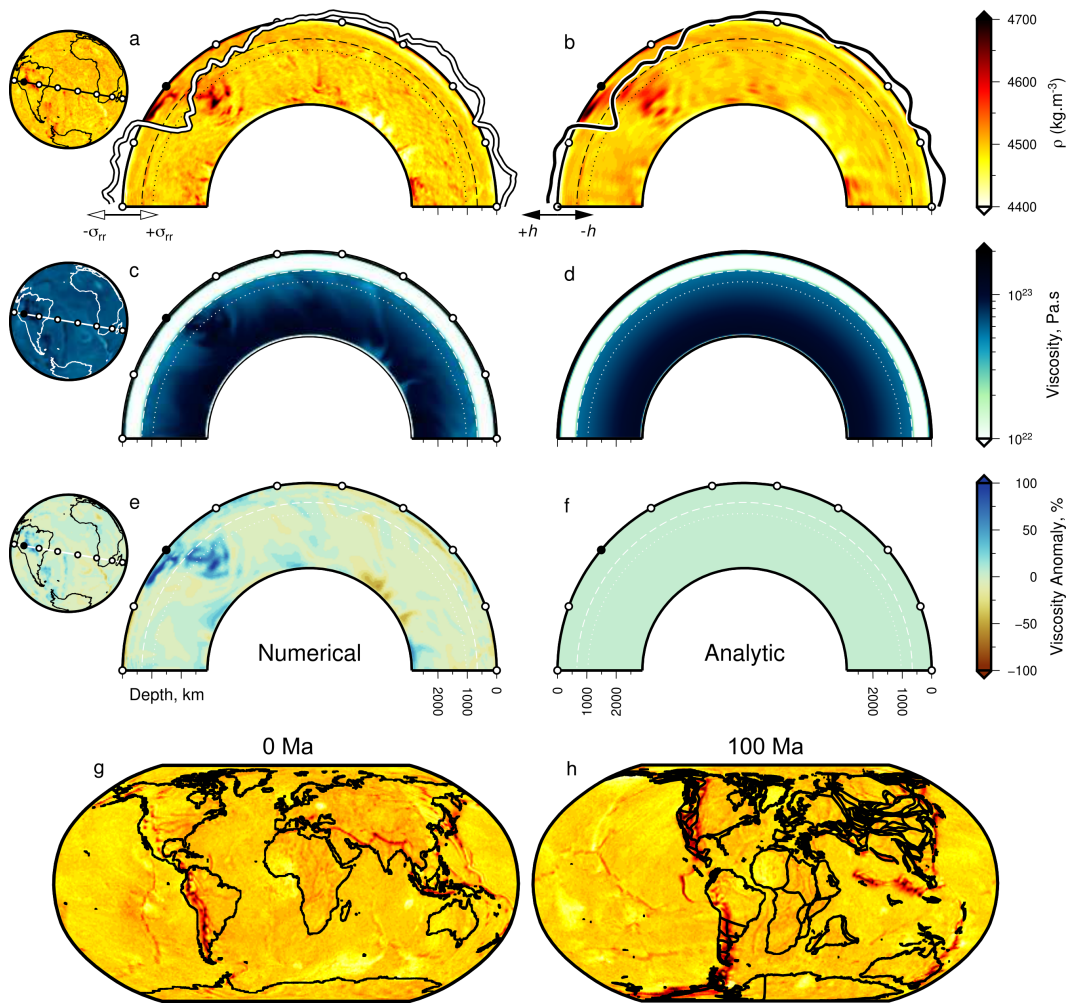


Figure 1. Examples of mantle densities and viscosity used to calculate stresses and surface deflections numerically and analytically. (a) Great-circle slice (180°) through full-resolution, present-day, density ρ , predicted by numeric model TERRA with temperature dependent viscosity (Model 11a; see Table 1 and body text); see globe to left for location. White circles = 20° intervals; filled black circle indicates orientation of cross section; dashed line = 660 km depth contour; dotted line = 1038 km depth contour, at which depth ρ is plotted on globe; white-black curve = numeric prediction of surface normal stress σ_{rr} from Model 11a. (b) As (a) but slice is through spherical harmonic expansion of density structure, to maximum degree $l = 50$ ($\lambda \approx 792$ km; Model 11b); black-white curve = surface deflection h , calculated using (analytic) propagator matrix approach (Model 12). (c) As (a) but for slice through full-resolution viscosity structure of numeric model. (d) As (c) but for mean (radial) viscosity structure, used along with the density structure shown in (b) to generate analytic solution for surface deflection shown by black-white curve atop (b). (e–f) As (c–d) but viscosity is expressed as a percentage anomaly with respect to the layer (radial) mean. (g–h) Predicted densities at 270 km depth at 0 and 100 Ma from numeric model with viscosity independent of temperature (Model 1a). Extended results are shown in Figure S1. Plate motions and paleo-coastlines are from Merdith et al. (2021).

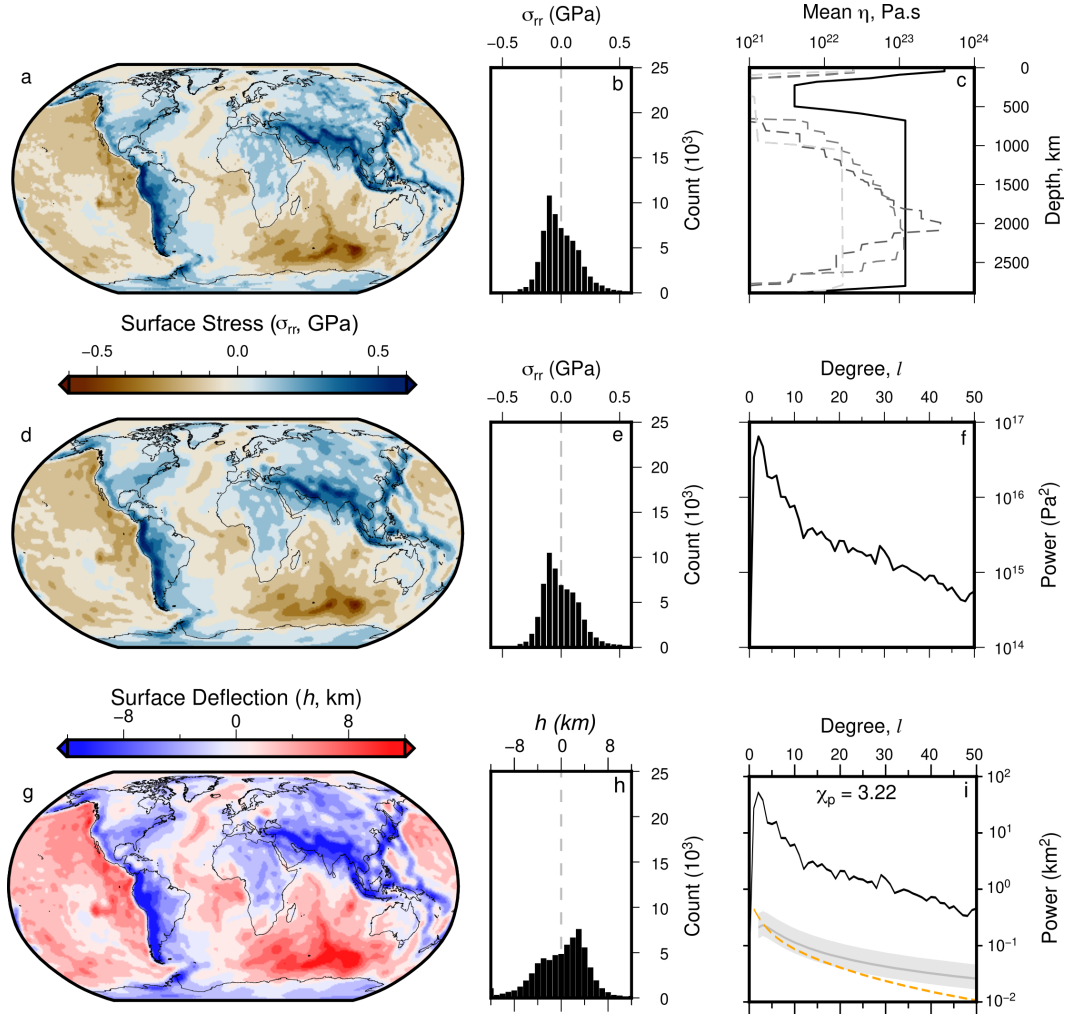


Figure 2. Surface stresses and deflections from numeric simulation of mantle convection with spherical harmonic expansion up to degree 50. (a) Predicted present-day surface radial stress, σ_{rr} (Model 1a). (b) Histogram of values shown in (a). (c) Black line = radial viscosity structure used to drive Model 1a and thus produce grid shown in panel (a). Gray dashed lines = alternative viscosity profiles of (from darkest to lightest) Mitrovica and Forte (2004), Steinberger and Calderwood (2006), and μ_1, μ_2 from Ghelichkhan et al. (2021). (d) Model 1b: Spherical harmonic fit to Model 1a (panel a) up to maximum degree $l = 50$ (minimum wavelength $\lambda \approx 792$ km). (e) Histogram of values shown in panel (d). (f) Power spectrum—total power per degree—of stress field shown in panel (d). (g) Spherical harmonic fit to surface deflections (Model 1b; up to degree $l = 50$). (h) Histogram of values shown in panel (g). (i) Black curve = power spectrum of calculated water-loaded surface deflections (panel g); gray line and band = expected dynamic topography from Kaula's rule using admittance $Z = 12 \pm 3$ mGal km^{-1} (Kaula, 1963). Orange dashed line = expected power spectrum for water-loaded residual topography (from Holdt et al., 2022) via analytic solution of special case of Equation 15. $\chi_p =$ root-mean-squared difference between calculated (black) and independent (orange & grey) surface deflection power (see Equation 20). All histograms are weighted by latitude to correct to equal-area. Figure S2 shows extended results including air-loaded deflections.

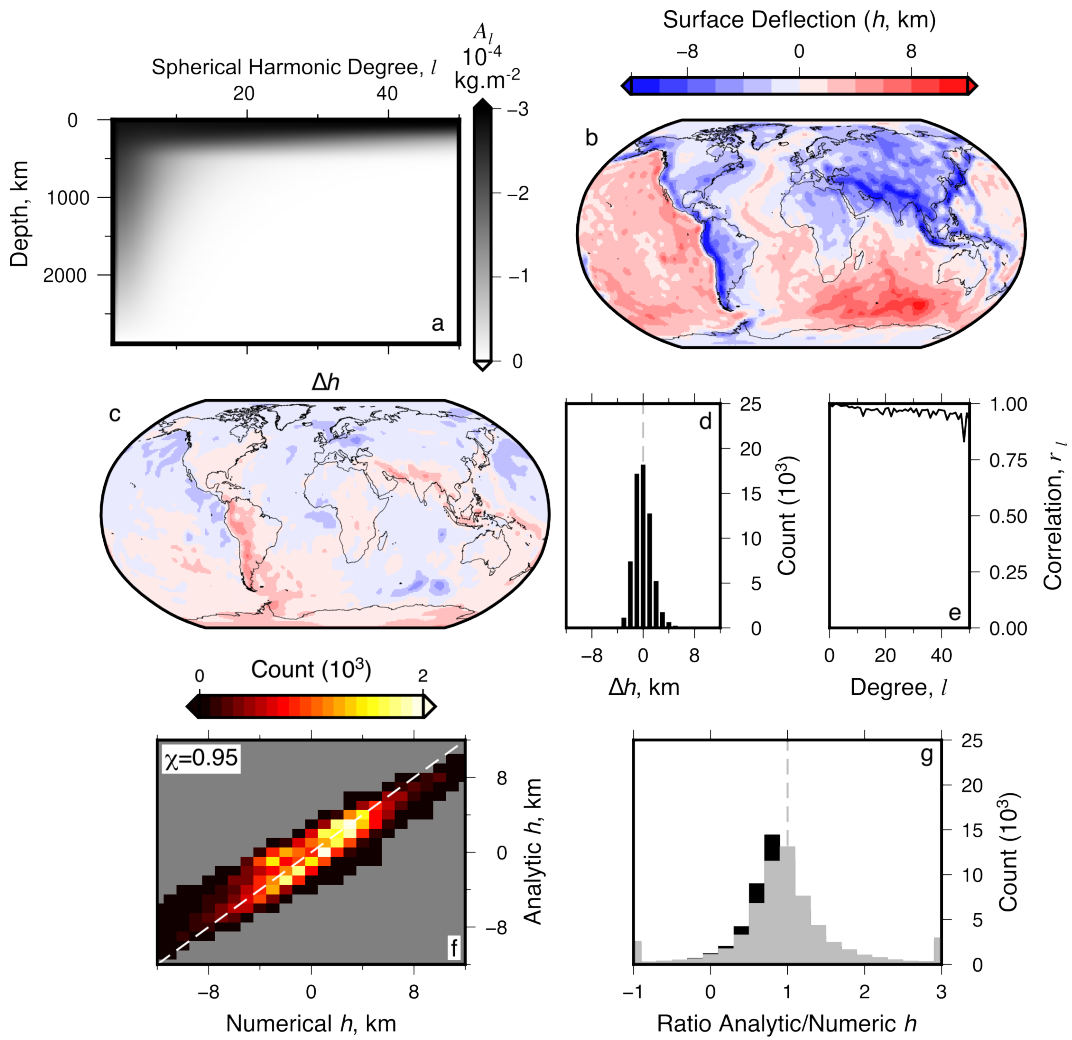


Figure 3. Comparisons of numeric (Model 1b) and analytic (Model 2) estimation of surface deflections from models with identical parameterization. (a) Surface deflection sensitivity kernel A_l as a function of spherical harmonic degree, l , and depth (Model 2). (b) Propagator matrix (analytic) solution for water-loaded surface deflection calculated using sensitivity kernel shown in panel (a). Figure S3 shows extended results including power spectra and air-loaded deflections. (c) Difference, Δh , of surface deflections in Models 1b and 2. (d) Histogram of difference values shown in (c). (e) Spectral correlation coefficient, r_l , between Models 1b and 2; Equation 8. (f) Comparison of predicted surface deflections; χ = root-mean-squared difference between predictions (Equation 7); gray dashed line = 1:1 ratio. (g) Black bars = histogram of ratios between analytic:numeric solutions for surface deflection as in (f). Gray dashed line = 1 (i.e., identical values). Gray bars = as black bars, but for propagator matrix solution amplitudes scaled up by optimal factor to fit numeric solution (=10%). All histograms are weighted by latitude to correct to equal-area.

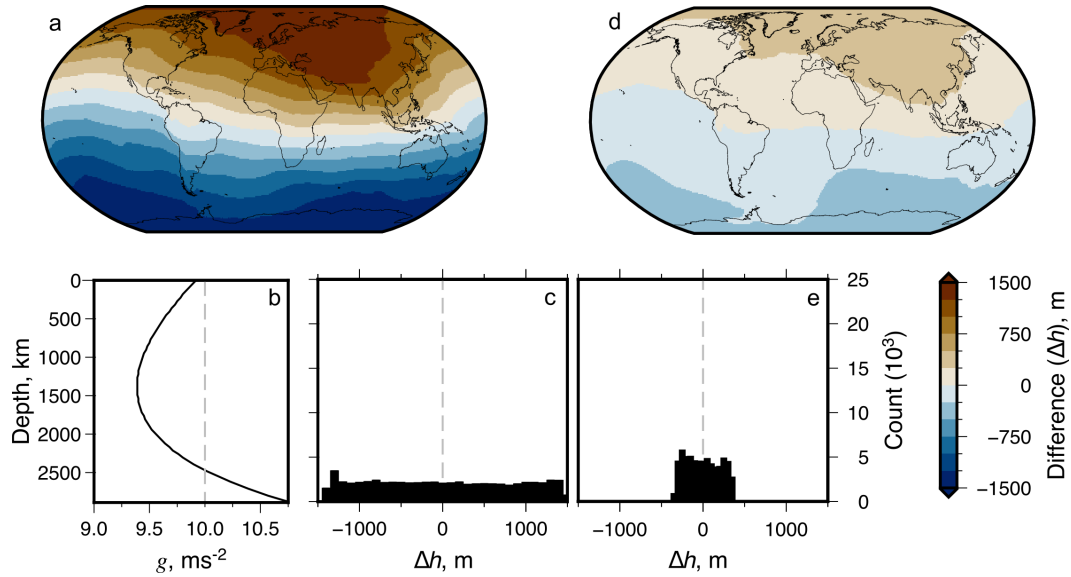


Figure 4. Impact of self-gravitation (a–c) and gravitational potential of deflected surfaces (d–e) on surface deflections calculated analytically. In these tests surface deflections from models with different gravity parameterizations are compared to predictions from Model 2. (a) Difference between water-loaded surface deflections calculated using the propagator matrix technique incorporating self-gravitation (Model 3; black curve in panel b) and $g = 10 \text{ m s}^{-2}$ (dashed line in panel b; Model 2). (c) Histogram of values in panel (a). (d–e) Differences in surface deflection from models with (Model 4) and without (Model 2) stress perturbations induced by gravitational potential of the deflected surface. All histograms are weighted by latitude to correct to equal-area, they show the full extent of the results. Figures S4–S5 show extended results including maps of calculated surface deflections.

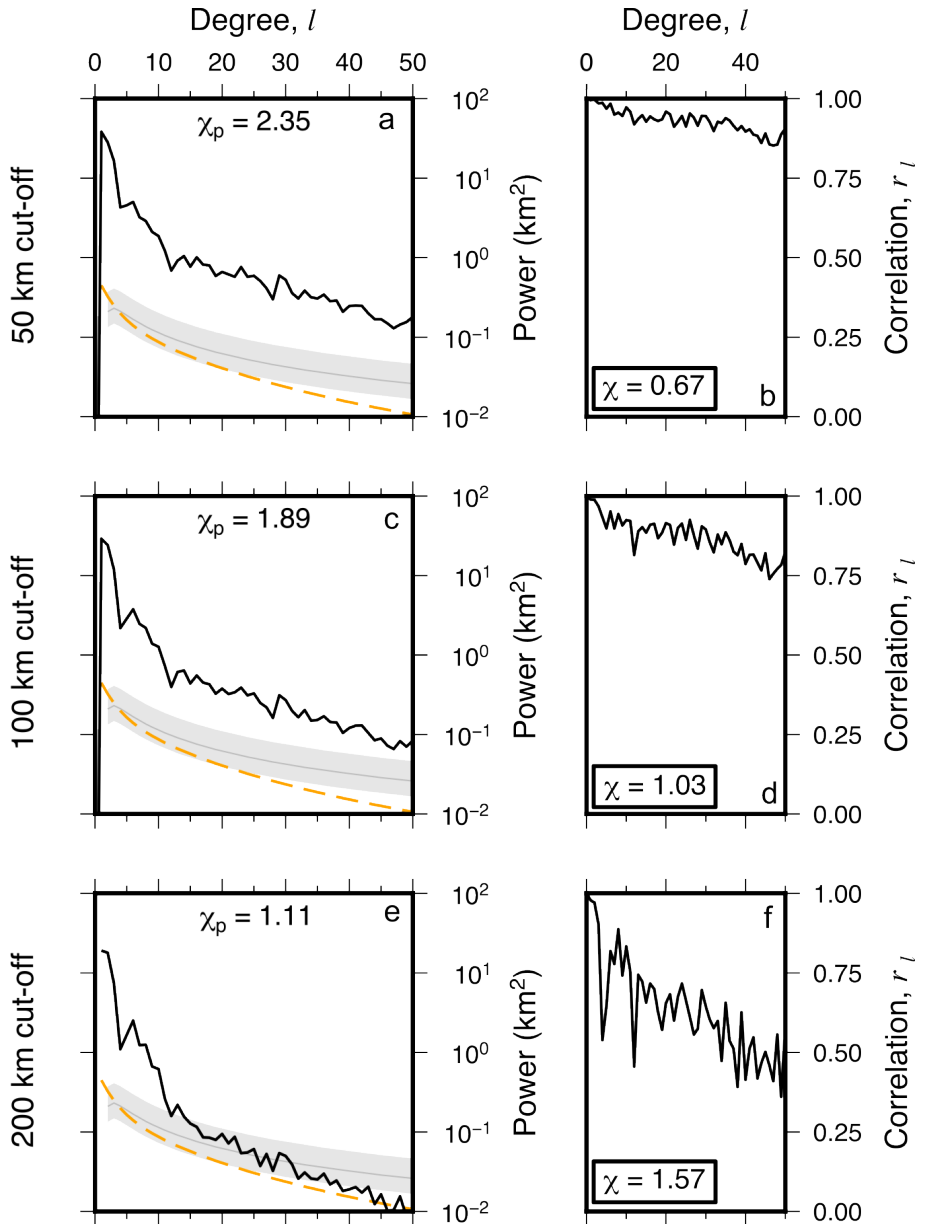


Figure 5. Effect of removing shallow structure on surface deflections calculated analytically. Surface deflections in models with shallow structure removed are compared to those predicted by Model 2. (a) Black line = Power spectra of predicted water-loaded surface deflection from propagator matrix solution for Model 2 (Figure 3b), but with effect of upper 50 km of density anomaly structure ignored in calculation (Model 5). Gray line and band = expected dynamic topography from Kaula's rule using admittance $Z = 12 \pm 3 \text{ mGal km}^{-1}$ (Kaula, 1963). Orange dashed line = expected power spectrum for water-loaded residual topography from Holdt et al. (2022), via analytic solution of special case of Equation 15. χ_p = root-mean-squared difference between calculated (black) and independent (orange & grey) surface deflection power (see Equation 20). (b) Spectral correlation coefficient, r_l , of surface deflections in Models 5 and 2 (see Equation 19). Inset χ = root-mean-squared difference in surface deflections of Models 5 and 2 (see Equation 18). (c-d) and (e-f) as (a-b) but for depth cut-offs of 100 (Model 6) and 200 km (Model 7), respectively. Figure S7 show extended results including maps of calculated surface deflections and differences with Model 2.

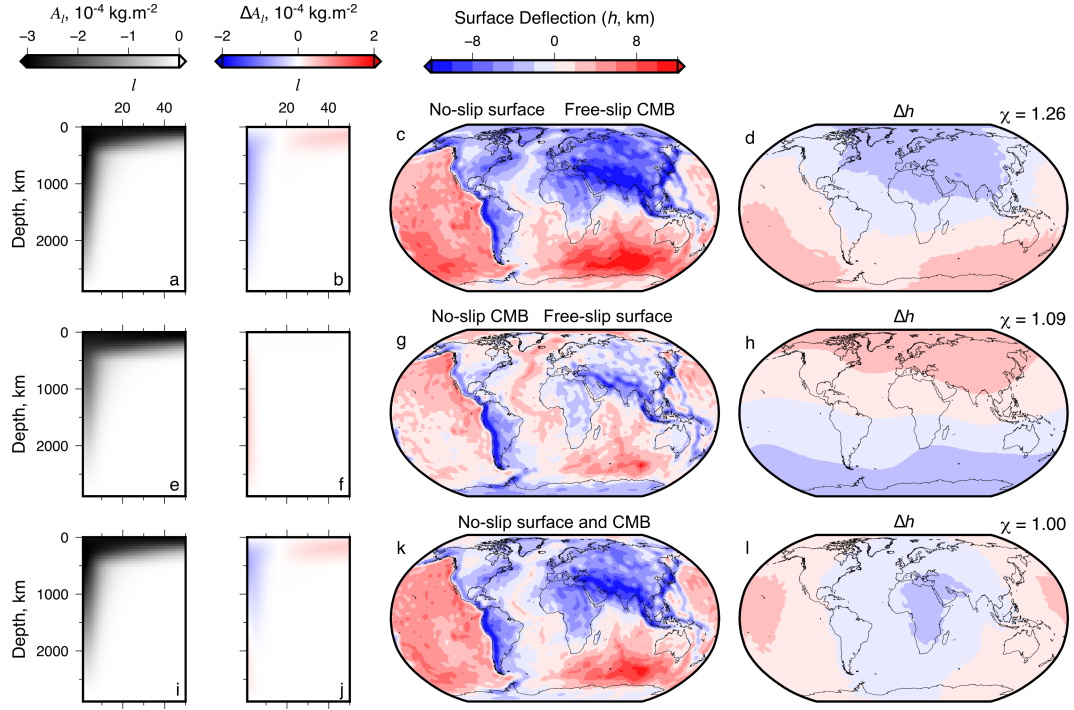


Figure 6. Impact of free- and no-slip surface and core-mantle boundary boundary conditions on surface deflections. This figure shows comparisons of surface deflections from models with different assumed boundary conditions and Model 2. (a) Water-loaded surface deflection sensitivity kernel A_l , for Model 8, which has a no-slip surface boundary condition, but otherwise is parameterised the same as Model 2. (b) Sensitivity kernel of Model 8 minus sensitivity kernel of Model 2. Note, positive difference implies reduced sensitivity compared to Model 2, and vice versa, since A_l is negative. (c) Predicted water-loaded surface deflection for Model 8. (d) Difference between surface deflection predictions for Model 8 and Model 2. (e–h) as (a–d) but for Model 9: free-slip surface boundary, no-slip CMB. (i–l) as (a–d) but for Model 10: no-slip surface and CMB boundaries.

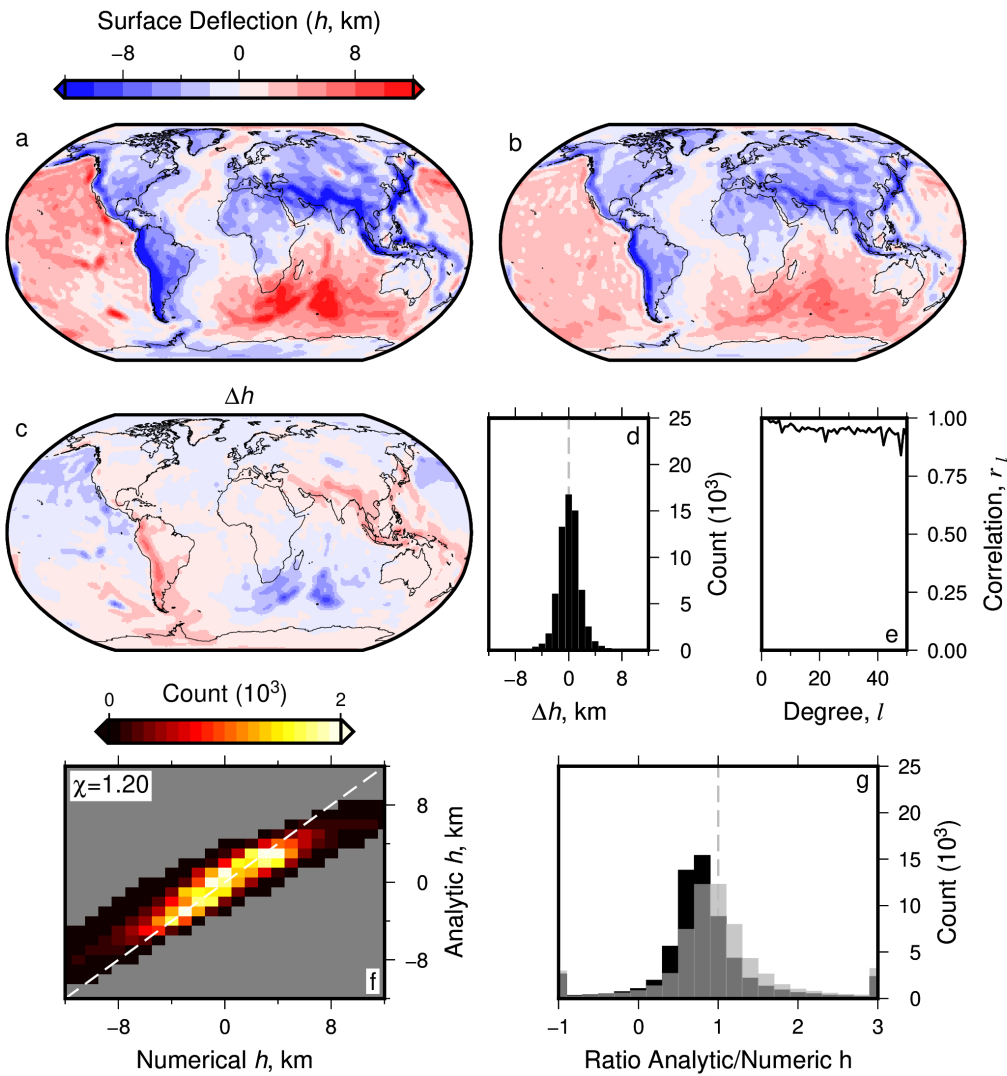


Figure 7. Comparison of surface deflections calculated numerically (Model 11b) and analytically (Model 12) using results from simulation with temperature dependent viscosity. (a) Model 11b: Spherical harmonic expansion of predicted present-day water-loaded surface deflection converted from stress output from numeric model TERRA (Model 11a), to maximum degree $l = 50$. (b) Model 12: As (a) but for prediction made using propagator matrix method. (c) Difference, Δh , between Models 11b and 12 (panels a and b). (d) Histogram of difference values shown in (c), weighted by latitude to correct to equal-area. (e) Spectral correlation coefficient, r_l , between predictions shown in panels (a) and (b); Equation 8. (f) Numeric (Model 11b) versus analytic (Model 12) predictions of surface deflection; χ = root-mean-squared difference between predictions, Equation 7; gray dashed line = 1:1 ratio. (g) Histogram of ratios between analytic:numeric solutions for surface deflection as in (f), weighted by latitude. Gray dashed line = 1 (i.e., identical values). Gray bars = as black bars, but for propagator matrix solution amplitudes scaled up by optimal factor to fit numeric solution (24%).

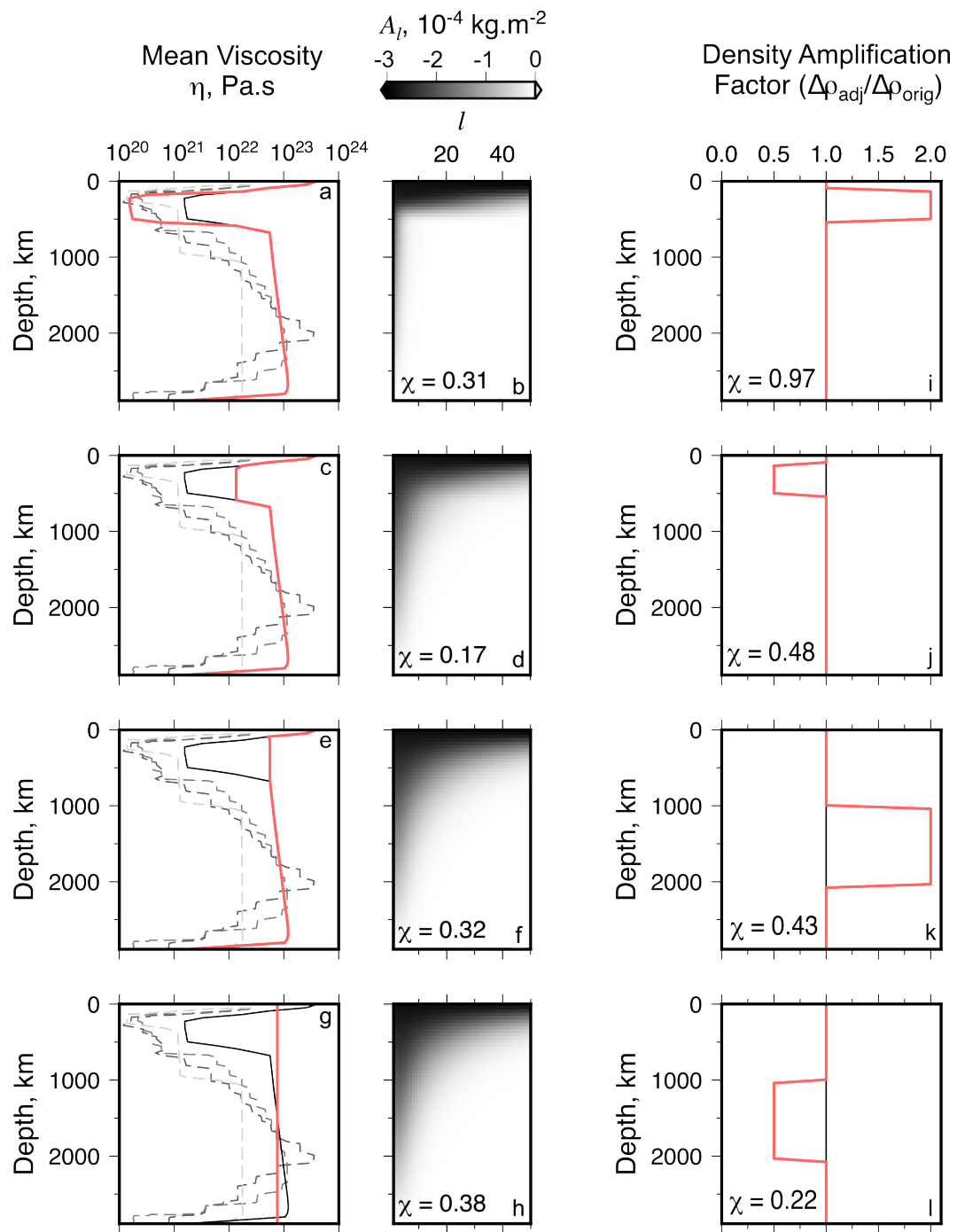


Figure 8. Sensitivity of calculated analytic surface deflection to adjusted radial viscosity (a–h) and density anomalies (i–l). This figure shows comparisons of surface deflections calculated in models with modified viscosity and density to the results from Model 12 (see Table 1). (a) Black curve = unadjusted prediction of present-day radial mean viscosity from Model 11; red line = adjusted radial profile with viscosity decreased by a factor of 10 between depths of $\sim 300\text{--}500$ km (Model 13); gray dashed lines = viscosity profiles used in other studies (see Figure 2). (b) Sensitivity kernel for the viscosity profile indicated by the red curve in panel a. Value of root-mean-squared difference, χ , between calculated surface deflections for unadjusted and adjusted viscosity is stated (see Equation 7). (c–h) Results from testing alternative radial viscosity (Models 14–16). Figure S13 shows extended results including maps of surface deflections and their differences. (i–l) Density anomalies (red line) adjusted by directly scaling spherical harmonic coefficients ($l > 0$) up or down by a factor of 2 (Models 17 & 19: panels e & g) or $\frac{1}{2}$ (Models 18 & 20: f & h). Viscosity structure applied in each case is same as that used to generate Figure 7b. Sensitivity kernels for surface deflections are not shown since they are invariant with respect to density anomalies, $\Delta\rho$, depending only on viscosity structure. Figure S14 shows extended results including maps of surface deflections and their differences.

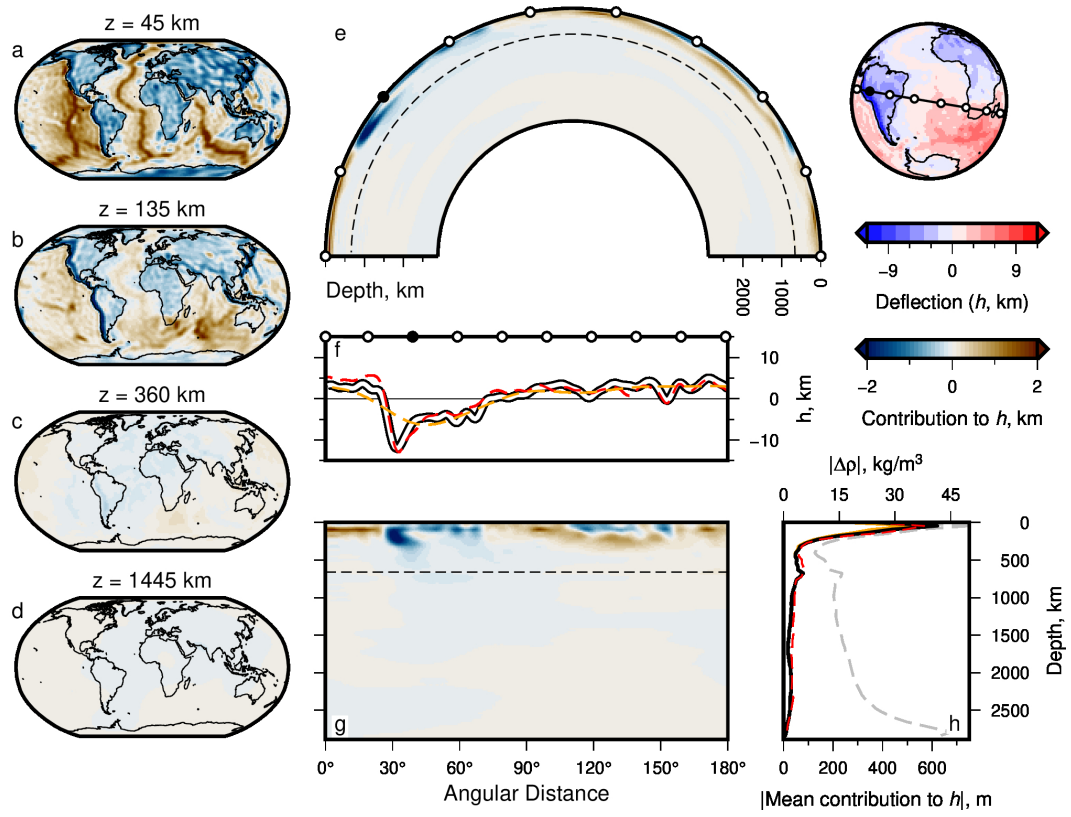


Figure 9. Effective density; contributions from density anomalies to surface deflection. (a–d) Maps of net contribution to present-day water-loaded surface deflection calculated using propagator matrix approach (Model 12; see body text for details). Depth slices at 45, 135, 360 and 1445 km depth incorporating all spherical harmonic degrees l and orders m , up to $l = 50$. (e) Great-circle slice (180°) showing contributions to surface deflection; globe to right shows transect location and calculated surface deflection (Model 12). White circles = 20° intervals; note filled black circle for orientation; dashed line = 660 km depth contour. (f) White-black curve = total surface deflection along transect shown atop globe in panel (e); abscissa aligned with panel g; orange dashed line = same but for maximum $l = 10$ (see Supporting Information Figure S18); red dashed curve = surface deflection from Model 2. (g) Cartesian version of panel (e); ordinate aligned with panel (h). (h) Grey dashed curve = mean absolute value of density anomalies in Model 12—see top axis for values. Black curve = global mean amplitude (modulus) of contribution from density structure in Model 12 to total surface deflection h , across all l and m ; orange line = same but for maximum $l = 10$; red dashed line = results for Model 2 (see Section 6.3). See Figures S15–S19 for extended results, demonstrating sensitivity of surface deflections to maximum spherical harmonic degree.